MNRAS 000, 1–20 (2016) Preprint 12 April 2016 Compiled using MNRAS LATEX style file v3.0

The Nature of Hβ+[OIII] and [OII] emitters to $z \sim 5$ with HiZELS: stellar mass functions and the evolution of EWs

A. A. Khostovan[1]⋆, D. Sobral[2,3], B. Mobasher[1], I. Smail[4,5], B. Darvish[6], H. Nayyeri[7], S. Hemmati[8], J. P. Stott[9]

[1] *Department of Physics & Astronomy, University of California, Riverside, CA 92512, USA*
[2] *Department of Physics, Lancaster University, Lancaster, LA1 4YB, UK*
[3] *Leiden Observatory, Leiden University, PO Box 9513, NL-2300 RA Leiden, the Netherlands*
[4] *Centre for Extragalactic Astrophysics, Department of Physics, Durham University, Durham DH1 3LE, UK*
[5] *Institute for Computational Cosmology, Durham University, Durham DH1 3LE, UK*
[6] *Cahill Center for Astronomy and Astrophysics, California Institute of Technology, Pasadena, CA 91125, USA*
[7] *Department of Physics & Astronomy, University of California, Irvine, CA 92697, USA*
[8] *Infrared Processing and Analysis Center, California Institute of Technology, Pasadena, CA 91125, USA*
[9] *Sub-department of Astrophysics, Department of Physics, University of Oxford, Oxford OX1 3RH, UK*

arXiv:1604.02456v1 [astro-ph.GA] 8 Apr 2016

ABSTRACT

We investigate the properties of ∼ 7000 narrow-band selected galaxies with strong Hβ+[OIII] and [OII] nebular emission lines from the High-z Emission Line Survey (HiZELS) between $z \sim 0.8 - 5.0$. Our sample covers a wide range in stellar mass ($M_{\rm stellar} \sim 10^{7.5-12.0}$ M$_\odot$), rest-frame equivalent widths (EW$_{\rm rest}$∼ 10 – 10^5 Å), and line luminosities ($L_{\rm line} \sim 10^{40.5-43.2}$ erg s^{-1}). We measure the Hβ+[OIII]-selected stellar mass functions out to $z \sim 3.5$ and find that both $M_\star$ and $\phi_\star$ increases with cosmic time, which may be due to the [OIII] selection including an increasing fraction of AGN at lower redshifts. The [OII]-selected stellar mass functions show a constant $M_\star \approx 10^{11.6}$ M$_\odot$ and a strong, increasing evolution with cosmic time in $\phi_\star$ in line with Hα studies. We also investigate the evolution of the EW$_{\rm rest}$ as a function of redshift with a fixed mass range ($10^{9.5-10.0}$ M$_\odot$) and find an increasing trend best represented by $(1+z)^{3.81\pm0.14}$ and $(1+z)^{2.72\pm0.19}$ up to $z \sim 2$ and $z \sim 3$ for Hβ+[OIII] and [OII] emitters, respectively. This is the first time that the EW$_{\rm rest}$ evolution has been directly measured for Hβ+[OIII] and [OII] emitters up to these redshifts. There is evidence for a slower evolution for $z > 2$ in the Hβ+[OIII] EW$_{\rm rest}$ and a decreasing trend for $z > 3$ in the [OII] EW$_{\rm rest}$ evolution, which would imply low [OII] EW at the highest redshifts and higher [OIII]/[OII] line ratios. This suggests that the ionization parameter at higher redshift may be significantly higher than the local Universe. Our results set the stage for future near-IR space-based spectroscopic surveys to test our extrapolated predictions and also produce $z > 5$ measurements to constrain the high-z end of the EW$_{\rm rest}$ and [OIII]/[OII] evolution.

Key words: galaxies: evolution – galaxies: fundamental parameters – galaxies: high-redshift – galaxies: mass function – galaxies: star formation – cosmology: observations.

1 INTRODUCTION

In the past two decades, great strides have been made in understanding the evolution of observed properties of star-forming galaxies across cosmic time. We now know that the peak of star formation activity occurred somewhere between $z \sim 2$ and 3 (e.g., Karim et al. 2011; Bouwens et al. 2012a,b; Cucciati et al. 2012; Gruppioni et al. 2013; Sobral et al. 2013a; Bouwens et al. 2015; Khostovan et al. 2015) and that the majority of the stellar mass assembly occurred by $z \sim 1$ (e.g., Pérez-González et al. 2008; Marchesini et al. 2009; Ilbert et al. 2013; Muzzin et al. 2013; Madau & Dickinson

⋆ E-mail: akhostov@gmail.com

© 2016 The Authors

2014; Sobral et al. 2014; Tomczak et al. 2014; Grazian et al. 2015). Furthermore, recent spectroscopic surveys are giving us valuable insight on the physical properties of star-forming regions in the high-z Universe (e.g., Liu et al. 2008; Swinbank et al. 2012; Nakajima et al. 2013; Sobral et al. 2013b; Nakajima & Ouchi 2014; Newman et al. 2014; Shirazi et al. 2014; Steidel et al. 2014; Stott et al. 2014; Hayashi et al. 2015; Sanders et al. 2016; Stott et al. 2016).

As galaxies age and undergo star-formation, the byproduct of their star-formation activity is their stellar mass build up. Therefore, determining and understanding the evolution of the stellar mass function (SMF) is crucial as measuring the distribution of stellar mass within a given comoving volume provides important observational evidence on how galaxies may grow due to star formation (e.g., van Dokkum et al. 2010; Bauer et al. 2013), mergers (e.g., Drory & Alvarez 2008; Vulcani et al. 2015), and environmental influences (e.g., Baldry et al. 2006; Bundy et al. 2006; Bolzonella et al. 2010; Peng et al. 2010; Sobral et al. 2011; Giodini et al. 2012; Darvish et al. 2015a; Mortlock et al. 2015; Davidzon et al. 2015; Sobral et al. 2016). Measurements of the SMFs also provide valuable constraints for theoretical models of the hierarchical assembly of dark matter halos (e.g., SMF-DM Halo Mass relationship; Conroy & Wechsler 2009; Behroozi et al. 2013; Furlong et al. 2015; Henriques et al. 2015; Rodriguez-Gomez et al. 2015; for a recent review article see Somerville & Davé 2015).

Another observational tracer of galaxy formation and evolution is the stellar mass density (SMD), which measures the total stellar mass within a specific range of masses (e.g., $> 10^9$ $M_\odot$) or full range (e.g., integrating the SMF from zero to infinity) per unit of comoving volume. By combining with other SMD measurements over a wide redshift range, the evolution of the SMD can be measured and reveal how galaxies assembled their stellar mass over cosmic time. In a compilation of the latest SMD measurements (e.g., Arnouts et al. 2007; Gallazzi et al. 2008; Pérez-González et al. 2008; Kajisawa et al. 2009; Li & White 2009; Marchesini et al. 2009; Yabe et al. 2009; Pozzetti et al. 2010; Caputi et al. 2011; González et al. 2011; Bielby et al. 2012; Lee et al. 2012; Reddy et al. 2012; Ilbert et al. 2013; Moustakas et al. 2013; Muzzin et al. 2013; Labbé et al. 2013), Madau & Dickinson (2014) showed a strong, increasing trend from $z \sim 8$ to $z \sim 1$, followed by a shallower, increasing trend from $z \sim 1$ to the present. This evolution is correlated with the cosmic star-formation rate density (SFRD) evolution, such that it is possible to model the SMD evolution based on the average SFRD evolution by taking its time integral (e.g., Sobral et al. 2013a; Madau & Dickinson 2014; Khostovan et al. 2015) and vice versa via the time derivative (e.g., Pérez-González et al. 2008).

Despite the various measurements that have provided a general indication of the SMF and SMD evolution, there are several caveats. For example, spectral energy distribution (SED) models and templates used to measure stellar masses can introduce systematic biases based on assumptions made in the fitting process and differing methodologies (Mobasher et al. 2015). Also, the separation based on galaxy types typically is based on empirically-derived colour-colour selection diagnostics (e.g., *BzK*, Daddi et al. 2004; *UVJ*, Williams et al. 2009), which can vary based on the data-set used (e.g., selection effects arising from sample and/or survey size and depth). Therefore, to make further progress we need a reliable, clean sample of a specific type of galaxies over a large comoving volume that can trace the SMF and SMD evolution from low-z to high-z using a single methodology.

Recently, there has been a great deal of focus on the evolution of the specific star-formation rate (sSFR), which is defined as the star-formation rate divided by the stellar mass (e.g., Stark et al. 2013; González et al. 2014; Marmol-Queralto et al. 2015; Faisst et al. 2016). Since the sSFR is in inverse units of time, it can be interpreted as a direct measurement of the timescale of stellar growth in individual galaxies and also as the ratio between the current and past star-formation activity. Recent studies have constrained the evolution within the $z < 2$ regime, finding that the sSFR increases from $z = 0$ to $z \sim 2$ (Noeske et al. 2007; Damen et al. 2009; Sobral et al. 2014).

However, the sSFR evolution is less constrained for $z > 2$. Reddy et al. (2012) measured the sSFR evolution between $z \sim 2-3$ and Stark et al. (2009) and González et al. (2010) extended the measurements for $z > 4$. In comparison with the $z < 2$ data, the observational data show the sSFR increasing from 0.3 to 2 Gyr^{-1} between $z = 0$ and $z \sim 2$. For $z > 2$, some early studies found that sSFR showed no significant evolution and is claimed to stay flat around ~ 2 Gyr^{-1} up to $z \sim 7$ (Stark et al. 2009; González et al. 2010). In contrast, theoretical studies predict that, for the case of cold gas accretion growth, the sSFR should be increasing as $(1+z)^{2.25}$ (Davé et al. 2011, 2012). Latest measurements from the high-resolution EAGLE simulation also predict an increasing sSFR with redshift (Furlong et al. 2015). An issue that can arise for the observational studies at $z > 4$ is that they do not take into account the effects of nebular emission lines in the SED fitting process. Strong lines can contaminate the *Spitzer* IRAC bands at these redshifts resulting in overestimating stellar masses (e.g., Schaerer & de Barros 2009, 2010; Nayyeri et al. 2014; Smit et al. 2014). Looking at ~ 1700 $z \sim 3-6$ Lyman break galaxies (LBGs), de Barros et al. (2014) found that about two thirds of their sample had detectable emission lines and by taking them into account when fitting the SED resulted in significantly different physical parameters. Recently, González et al. (2014) presented newer measurements of the sSFR with the nebular contamination accounted for and found an increase of a factor of ~ 2 in comparison to the Stark et al. (2009) and González et al. (2010) measurements, but still in conflict with theoretical predictions.

To correct the overestimation of stellar masses and sSFRs requires that the contamination of nebular emission lines is taken into account. One way of doing this is by measuring the trends in the rest-frame equivalent widths (EW_{rest}) of lines, which is a ratio between the flux of the emission-line and the stellar continuum flux. Studies have mapped out the $EW_{rest}(H\alpha)$ evolution up to $z \sim 2$ (e.g., Erb et al. 2006; Fumagalli et al. 2012; Sobral et al. 2014) while the $z > 2$ trend is still uncertain since Hα falls into the infrared at these redshifts. Recent measurements, using colour excess in the *Spitzer* IRAC bands at $> 3\mu$m that are claimed to only be attributed to nebular emission line contribution, have attempted to extend the measurements of the evolution out to $z \sim 6$ (e.g., Shim et al. 2011; Rasappu et al. 2015). Other studies measured $EW_{rest}(H\beta+[OIII])$ between $z \sim 6-8$ and, using a line ratio, converted to Hα to ex-

tend the mapping of the $EW_{rest}(H\alpha)$ evolution (e.g., Labbé et al. 2013; Smit et al. 2014, 2015). It should be noted that current studies are UV selected and are only sensitive to the most extreme line-emitters which can be detected in the broad-band photometry. Therefore, these measurements can be only treated as upper-limits. What we require are complete samples of emission-line selected sources (e.g., cover a wide-range in EW_{rest} that represents a typical emission-line galaxy) to properly measure the EW_{rest} evolution at $z > 2$. The lines that can be used are Hβ+[OIII][1] up to $z \sim 3$ and [OII] up to $z \sim 5$ (e.g., Khostovan et al. 2015).

Tracing the evolution of the equivalent width of nebular emission lines also provides valuable insight to the physical conditions of the HII regions and how those physical conditions evolve over cosmic time (e.g., Liu et al. 2008; Nakajima et al. 2013; Nakajima & Ouchi 2014; Hayashi et al. 2015; Kewley et al. 2015). For example, the [OIII]/[OII] ratio as measured by EW_{rest}([OIII])/EW_{rest}([OII]) can, in principle, tell us about the ionization parameter and the ionization state of the gas forming stars.

In this paper, we present our investigation of the evolution in SMF, SMD, and EW_{rest} using a large sample of Hβ+[OIII] and [OII] emission-line galaxies at $z \sim 1$–5 from the High-Redshift Emission-Line Survey (HiZELS) presented by Khostovan et al. (2015). Our results have implications in terms of the evolution in the EW_{rest} and sSFR, as well as the physical conditions of the gas in the HII regions that produces the nebular emission-lines. Our results also present an empirical evolution of the EW_{rest} that can be used to estimate the nebular emission line contamination in broad-band photometry when such photometry are used in determining key physical properties (e.g., stellar masses).

The paper is structured as follows: Section 2 describes the HiZELS sample used in this paper; Section 3 presents the stellar mass, SMF, and SMD determinations; Section 4 highlights the results of this paper with interpretations of the SMF, SMD, EW_{rest}, and [OIII]/[OII] evolutions; Section 5 summarizes the main results of our study.

Throughout this paper, we assume ΛCDM cosmology, with $H_0 = 70$ km s^{-1} Mpc^{-1}, $\Omega_\Lambda = 0.3$, and $\Omega_m = 0.7$. We assume a Chabrier (2003) IMF and correct the literature measurements when needed. All magnitudes are presented as AB magnitudes (Oke & Gunn 1983).

2 HIZELS SAMPLE

Our sample consists of Hβ+[OIII] and [OII] emitters selected based on narrow-band photometry from HiZELS (Geach et al. 2008; Sobral et al. 2009, 2012; Best et al. 2013; Sobral et al. 2013a) found in the COSMOS (Scoville et al. 2007) and UDS (Lawrence et al. 2007) fields. We refer the reader to Sobral et al. (2013a) for details on the initial selection of sources with narrow-band excess.

[1] The narrow-band filters used all have FWHMs of ∼ 130 – 210Å and can differentiate between Hβ and [OIII] emitters, but the broad-band filters used in selecting sources have FWHMs too large to separate the sample. Therefore, our Hβ+[OIII] samples are comprised of a combination of Hβ and [OIII], although Khostovan et al. (2015) and Sobral et al. (2015a) showed that the samples are dominated by [OIII] emitters.

The sample consists of 3475 Hβ+[OIII] emitters between $z = 0.84$ and 3.24 and 3298 [OII] emitters between $z = 1.47$ and 4.69 in discrete redshift slices (see Table 1) with the redshifts corresponding to the narrow-band filters used by Sobral et al. (2013a)[2]. Our sample is backed by 233 and 219 spectroscopic measurements for Hβ+[OIII] and [OII], respectively, that are from zCOSMOS (Lilly et al. 2007), the UDSz Survey (Bradshaw et al. 2013; McLure et al. 2013), Subaru-FMOS (Stott et al. 2013), Keck-DEIMOS/MOSFIRE (Nayyeri et al., in prep), PRIsm MUlti-object Survey (PRIMUS; Coil et al. 2011), and VIMOS Public Extragalactic Redshift Survey (VIPERS; Garilli et al. 2014). This sample is based on a large areal coverage of ∼ 2 deg^2 equating to a comoving volume coverage of ∼ 10^6 Mpc^3, which greatly reduces the effects of cosmic variance (see Sobral et al. 2015a; Stroe & Sobral 2015).

The selection of Hβ+[OIII] and [OII] emitters is discussed in Khostovan et al. (2015). In brief, we used the emission-line source catalog of Sobral et al. (2013a) to select galaxies with Hβ+[OIII] or [OII] emission lines by using a combination of selection criteria: spectroscopic redshifts, photometric redshifts, and colour-colour diagnostics (with priority given in that order). Sources that had detections in more than one narrow-band filter were also selected on the basis that their confirmation is equivalent to spectroscopic confirmation (e.g., finding [OII] in NB921 and Hα in NBH at $z = 1.47$; see Sobral et al. 2012).

The rest-frame equivalent widths of emission lines are calculated using the following relation:

$$EW_{rest} \approx \frac{F_L}{f_C} = \frac{\Delta\lambda_{NB}}{1+z} \frac{f_{NB} - f_{BB}}{f_{BB} - f_{NB}(\Delta\lambda_{NB}/\Delta\lambda_{BB})} \quad (1)$$

where NB and BB are the narrow-band and broad-band filters, respectively, $\Delta\lambda$ is the corresponding width of the filter, f is the corresponding flux measured in the filter, F_L is the flux of the nebular emission line, and f_C is the continuum flux. Figure 1 shows the distribution of rest-frame EWs and line luminosities of the Hβ+[OIII] and [OII] emitters. Our sample consists of rest-frame equivalent widths that are as low as ∼ 10 Å and as high as 10^5 Å and a luminosity range between $10^{40.5}$ and $10^{43.2}$ erg s^{-1}. We refer the reader to Khostovan et al. (2015) for details on how the line luminosities were computed.

3 METHODOLOGY

3.1 SED Fitting

We use the Multi-wavelength Analysis of Galaxy PHYSical properties (MAGPHYS) code of da Cunha et al. (2008) to fit the SEDs of our sources and determine physical properties, such as stellar masses, star-formation rates, and $E(B-V)$. da Cunha et al. (2008) designed the code to treat the infrared as two sub-components (birth clouds and diffuse ISM) using empirical relations from Charlot & Fall (2000) and assuming a balance between the stellar and

[2] We refer the reader to Sobral et al. (2013a) for information regarding the filter profiles, FWHMs, effective wavelengths, and all other inquiries regarding the properties of the narrow-band and broad-band filters used.

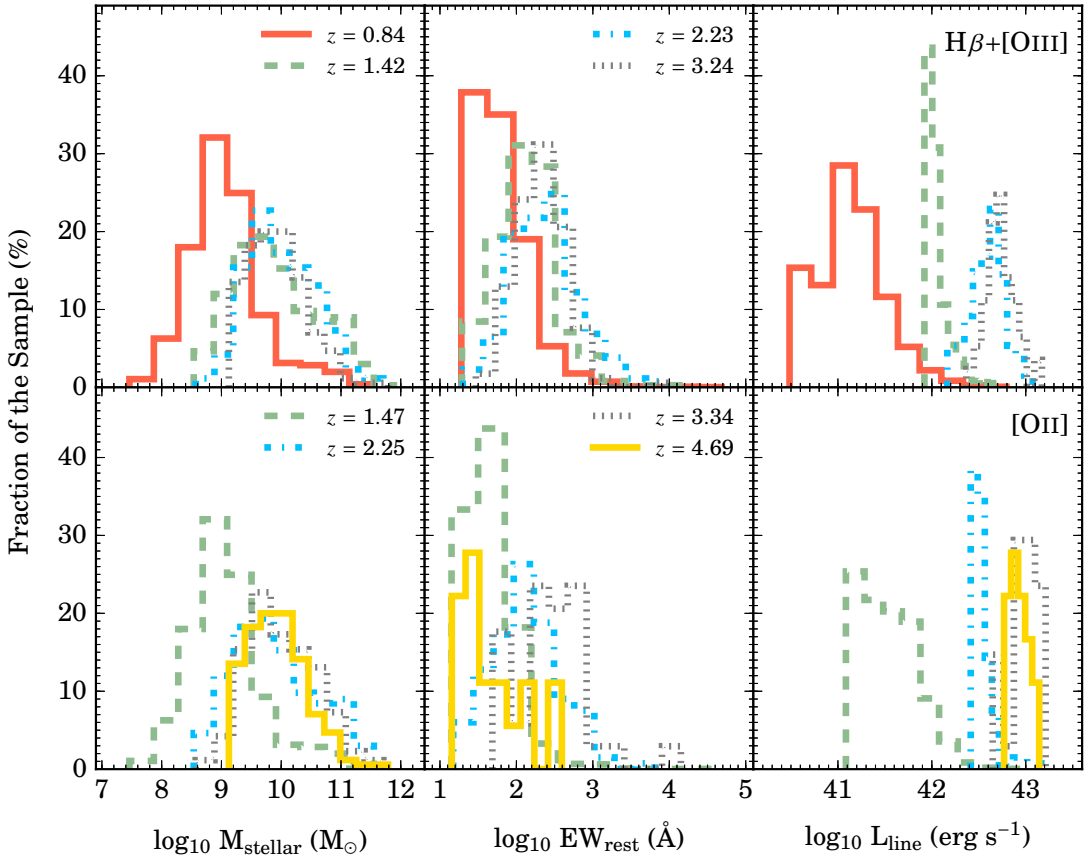

Figure 1. The stellar mass, EW_{rest}, and luminosity distributions for all of our samples. Based on the luminosity distributions, it is clear that our high-z sample is limited to high line luminosities ($L > 10^{42}$ erg s^{-1}). Our lowest redshift sample is the deepest and covers a wider luminosity, stellar mass, and EW_{rest} range which allows us to utilize the sample for tests of selection effects that can bias results at higher redshift.

dust/infrared components (e.g., the amount of attenuation in the stellar component is accounted for in the dust/infrared component).

MAGPHYS uses different model templates for the stellar and infrared components. The stellar component is generated by the Bruzual & Charlot (2003) code, while the infrared component templates are formed based on the prescription of Charlot & Fall (2000). We note that MAGPHYS assumes a Chabrier (2003) IMF[3]. The stellar templates include (1) exponentially declining star-formation histories $e^{-t/\tau}$ with τ in the range between 0.1 to 13.5 Gyr; (2) metallicities between 0.02 and 2 $Z_{\odot}$; and (3) dust attenuation based on Charlot & Fall (2000). MAGPHYS then fits the observed SEDs and creates marginalized likelihood distributions of physical parameters.

We fit the SEDs using *GALEX FUV* and *NUV*, CFHT Megaprime u^*, Subaru SuprimeCam $Bg'Vr'i'z'$, UKIRT WFCAM J and K, and *Spitzer* IRAC 3.6 - 8.0 μm photometry for our COSMOS sources. The SEDs of our UDS sources are fitted using CFHT MegaCam u, Subaru SuprimeCam $BVr'i'z'$, UKIRT WFCAM $YJHK$, and *Spitzer* IRAC 3.6 - 8.0 μm photometry. The outputs used in this study are the stellar masses. We use the COSMOS-30 i-band selected catalog (Capak et al. 2007; Ilbert et al. 2009) and the DR8 release of the Subaru-XMM-UKIDSS UDS K-band selected catalog (e.g., Cirasuolo et al. 2007; Lawrence et al. 2007). We refer the reader to the cited catalog papers for detailed descriptions of the multi-wavelength photometry.

We note that MAGPHYS was created to incorporate the 912 Å $< \lambda <$ 1 mm rest-frame range such that we have no mid- and far-infrared constraints. The unique part about MAGPHYS is that it fits the stellar and infrared/dust templates separately, such that in the case where there are no infrared constraints, the measurements will be based off of the fits using only the stellar templates. Furthermore, MAGPHYS does not have a prescription to incorporate the effects of nebular emission in the fitting process. Past studies have shown that nebular emission contamination can affect the stellar mass measurements from SED fitting (e.g., Schaerer & de Barros 2009; de Barros et al. 2014). As shown in Figure 1, we find that for the vast majority of our sources, their EW_{rest} are low enough ($< 10^3$ Å; e.g., Smit et al. 2014)

[3] To make our results comparable with other studies in the literature that utilize different IMFs, we state the conversions to the Salpeter IMF (+0.215 dex) and the Kroupa IMF (−0.04 dex).

and have $\sim 10-15$ individual photometric measurements for which the effects of nebular emission line contamination are negligible.

3.2 Stellar Masses

Figure 1 shows the range in stellar mass that were measured from MAGPHYS for all our samples. We find that our $z > 1$ Hβ+[OIII] emitters and $z > 1.5$ [OII] emitters have typical stellar masses $M_{\rm stellar} \sim 10^{9.5} - 10^{10}$ M$_\odot$. The $z = 0.84$ Hβ+[OIII] and $z = 1.47$ [OII] samples have distributions that peak at lower masses ($M_{\rm stellar} \sim 10^{8.5} - 10^{9}$ M$_\odot$) and cover a wider range ($M_{\rm stellar} \sim 10^{7.5} - 10^{12.0}M_\odot$). Both samples come from NB921 observations, which, as seen in the luminosity distributions shown on Figure 1, probe deeper than all the other samples, but also covers a much smaller volume ($\sim 3-7\times10^5$ Mpc^{-3}, Khostovan et al. 2015). Since the COSMOS field has a wealth of multi-wavelength with measurements of stellar masses, we make a comparison between our measurements and those of Ilbert et al. (2010) and Muzzin et al. (2013) as shown in Appendix B. We find that our measurements are consistent with those of the literature.

3.3 Creating Stellar Mass Functions

We create stellar mass functions by using a similar approach as in Khostovan et al. (2015) by applying the $V_{\rm max}$ estimator where the data is binned as such:

$$\phi(M_j) = \frac{1}{\Delta M_j} \sum_{i=0}^{N} \frac{1}{C(M_i) V_{{\rm max},i}} \quad (2)$$

where M_j is the $j^{\rm th}$ mass bin, ΔM_j is the bin-size, and $C(M_i)$ is the completeness and $V_{\rm max,i}$ is the volume for the $i^{\rm th}$ source in the $j^{\rm th}$ bin. The masses, M, used in this equation are all in log-scale.

3.3.1 Completeness Correction

All the stellar mass functions have been corrected for completeness based on the completeness corrections determined by Khostovan et al. (2015) using the approach of Sobral et al. (2013a, 2014). We adopt this approach for correcting our SMFs because our samples are flux- and EW-limited and not mass-limited. Therefore, we need to correct based on the line flux and EWs as this is where the incompleteness arises. In brief, the completeness correction takes into account the full selection function (including the EW$_{\rm rest}$ cut and the difference in luminosity limits/depths between one sub-field and another) in terms of line luminosity. Furthermore, we applied a volume/filter profile correction (see Khostovan et al. 2015), which takes into account the loss of flux at the wings of the narrow-band filters. We also applied an EW$_{\rm rest}$ completeness correction to take into account the missing number of high mass galaxies in our $z = 0.84$ SMF. This is described in detail in Appendix C.

3.3.2 Common Relative Luminosity Cut

As seen in Figure 1, each sample covers different line luminosities making it difficult to directly compare samples. Furthermore, the volumes probed per each sample are different where the lowest redshift samples have comoving volumes of $\sim 3-6\times10^5$ Mpc^3 and the highest redshift samples with $\sim 10-16\times10^5$ Mpc^3 (Khostovan et al. 2015). This raises problems in terms of compatibility for comparison as the line luminosity and volume differences can capture different populations of galaxies. In order to solve this issue, we use a similar approach to Sobral et al. (2014) by placing a common $L/L_\star(z)$ limit to make the samples directly comparable using the $L_\star(z)$ measurements of Khostovan et al. (2015). This is accomplished by comparing the distribution of sources per redshift in terms of their $L/L_\star(z)$ ratio where we find that the common limit for Hβ+[OIII] is $\sim 0.4L_\star(z)$ and for [OII] it is $\sim 0.85L_\star(z)$ (see Table 3 of Khostovan et al. 2015 for the $L_\star(z)$ measurements). Disregarding this common limit will result in stellar mass functions and densities that trace different types of emitters.

z	$L_\star$ (erg s^{-1})	$N_{\rm total}$	$N_{\rm sel}$	Fraction
Hβ+[OIII] ($L > 0.4L_\star(z)$)				
0.84	41.79	2477	524	21%
1.42	42.06	371	371	100%
2.23	42.66	271	256	95%
3.24	42.83	179	175	98%
[OII] ($L > 0.85L_\star(z)$)				
1.47	41.86	3285	676	21%
2.25	42.34	137	137	100%
3.34	42.69	35	35	100%

Table 1. To ensure compatibility between different redshift samples, we apply a common $L/L_\star(z)$ cut (Hβ+[OIII]: $L > 0.4L_\star(z)$ and [OII]: $L > 0.85L_\star(z)$ where the $L_\star(z)$ measurements are from Khostovan et al. (2015). For each redshift sample, we highlight the total number of emitters in the sample ($N_{\rm total}$), the total number of emitters selected after the $L/L_\star(z)$ cut ($N_{\rm sel}$), and the corresponding fraction of emitters selected.

This consequentially reduces the sample size, especially for the lowest z samples ($z \sim 0.84$ for Hβ+[OIII] and $z \sim 1.47$ for [OII]) as they are the deepest and have the largest sample size. Table 1 shows the change in sample size when applying the common relative luminosity cut. Percentages shown correspond to the percentage of sources that were selected in comparison to the full sample. The NB921 samples (Hβ+[OIII] $z = 0.84$ and [OII] $z = 1.47$) saw the largest reductions in sample size due to their line luminosity distributions peaking at lower luminosities (see Figure 1 for the line luminosity distributions of all the samples). The higher-z samples retain the vast majority of their original sample sizes due to the fact that the lower $L/L_\star(z)$ limit chosen was on their line luminosity distributions.

3.4 Which one dominates: Hβ or [OIII]?

As mentioned in §2 and discussed in Khostovan et al. (2015), our Hβ+[OIII] sample is a combination of Hβ and [OIII] emitters. The narrow-band filters can differentiate between the different emission lines. The problem arises in the selection techniques used by Khostovan et al. (2015), which, as briefly described in §2, rely on a combination of spectroscopic con-

firmation, photometric redshifts, and colour-colour criteria. The photometric redshifts and colour-colour criteria both depend on using the multi-wavelength broad-band filters data sets, which results in the Hβ and [OIII] emitters to be blended with each other.

The important question that arises from this is which one dominates the Hβ+[OIII] sample: Hβ or [OIII] emitters? Khostovan et al. (2015) showed that the [OIII] line dominates the population of emitters with the fraction of Hβ emitters increasing with decreasing Hβ+[OIII] line luminosities. In a similar study, Sobral et al. (2015a) used their CF-HiZELS $z \sim 1.4$ sample from the ≈ 10 deg^2 SA22 field and found that $\sim 16\%$ of their spectroscopically confirmed Hβ+[OIII] emitters were Hβ emitters. Therefore, we can safely assume that the [OIII] emitters dominate our Hβ+[OIII] sample.

3.5 Contamination from AGNs

AGNs will also be selected with narrow-band surveys as the energetic UV photons they release can produce the emission lines that are also produced by the UV photons from bright, massive stars in star-forming, HII regions. Khostovan et al. (2015) and Sobral et al. (2015a) both studied the AGN contamination in their samples by using the 1.6μm bump as an observational proxy. Both found, on average, that the AGN contamination is $\sim 10-20\%$ of the total population. Khostovan et al. (2015) also compared the Hβ+[OIII] luminosity functions to the $z \sim 0.7$ zCOSMOS [OIII] type-2 AGN luminosity function of Bongiorno et al. (2010) and found that the brightest emitters in the Hβ+[OIII] sample are probable AGNs and as the Hβ+[OIII] line luminosity decreases, so does the fraction of AGN contribution.

We note that any type 1 (broad line) AGN in our sample may result in a poor χ^2 SED fits making them easier to remove from the sample. The type 2 (narrow line) AGNs are harder to remove but can still result in poor χ^2 fits. To remove this contamination, we incorporate a $\chi^2_{\rm reduced} < 100$.

4 RESULTS

4.1 Quiescent Population?

In the past, many studies used the rest-frame UVJ colour-colour selection to separate quiescent/passive and star-forming galaxies (eg., Williams et al. 2009; Brammer et al. 2011; Muzzin et al. 2013). Unobscured star-forming galaxies will have bluer rest-frame $U-V$ colours, corresponding to younger stellar populations and a lower or no 4000Å break, and also have bluer $V-J$ colours forming a locus within the UVJ plane. Dust-free quiescent galaxies are dominated by a more evolved stellar population resulting in a more pronounced 4000Å break, resulting in redder $U-V$ colours, although dust-obscured star-forming galaxies can occupy the same regime due to attenuation. This degeneracy is broken by $V-J$, where dust-free quiescent galaxies have bluer colours than the dust-obscured star-forming galaxies. The UVJ classification scheme does not take into account possibility of AGN contamination, such that galaxies that fall under both classifications can also be potential AGNs. Both classifications can also include sources with more complex spikes of obscured/unobscured star formation. We therefore refer to the quiescent classification as "passive" and the star-forming classification as "active" to take into account AGNs.

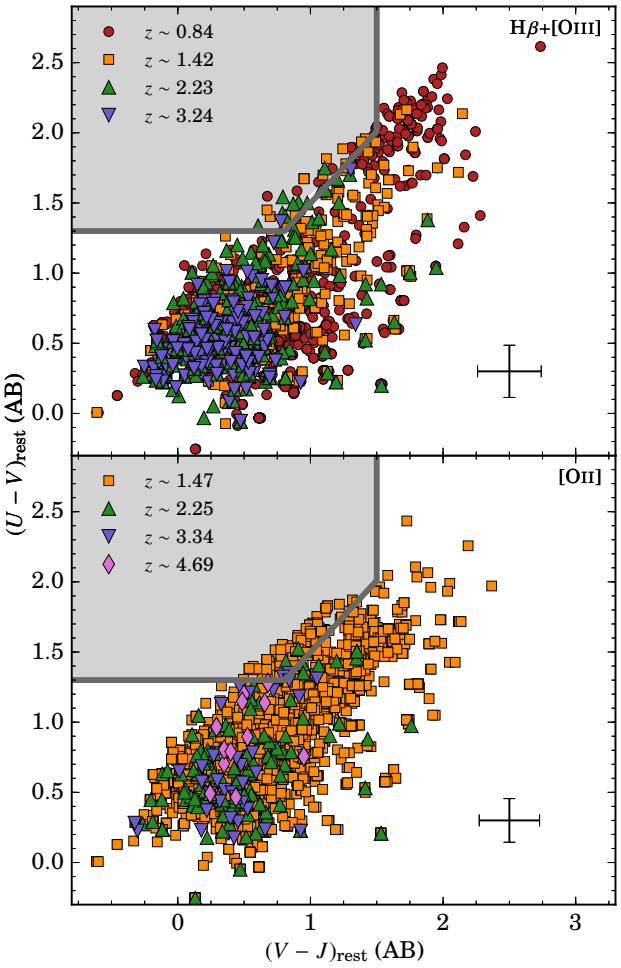

Figure 2. The UVJ colour-colour diagnostic used to separate star-forming galaxies from quiescent galaxies. The highlighted region and *grey* boundaries are the Muzzin et al. (2013) quiescent selection region. Included is the typical 1σ range for all sources per emission line. We find that the majority of our sources reside within the star-forming classification region. Sources that are within the quiescent region are consistent with photometric scatter. We find a general trend in the UVJ plane where high-z sources tend to have bluer rest-frame UVJ colours that could be caused by changes in dust and/or the star-formation efficiency (e.g., Papovich et al. 2015).

It must be noted that the UVJ selection is empirically driven and varies based on the data-set used, as well as the filters used in determining the rest-frame AB magnitudes. We apply the Muzzin et al. (2013) UVJ selection and use the same filters (Johnson U and V and 2MASS J) to study the nature of our sample. Figure 2 shows our full sample of emitters and the Muzzin et al. (2013) colour-colour selection. We include the 1σ range for all sources per emission

line that is calculated from the observed error bars of the corresponding *UVJ* observer-frame filters.

We find that, for all our Hβ+[OIII] and [OII] samples, > 98.5% are classified as active based on this selection criteria. We also find a small population of emitters that fall under the passive classification area. For the Hβ+[OIII] sample, only 0.8% (26 emitters) fall within this selection area with the majority ($\sim$ 38% of the 26 emitters) being from the $z \sim 1.42$ sample. The [OII] sample has a total of 2.4% (79 emitters) of the full sample within the passive selection region with the vast majority ($\sim$ 96%; 76 of the 79 emitters) coming from the $z \sim 1.47$ sample. These are mostly faint sources that fall into the passive selection region and are consistent with photometric scatter. Overall, the sources discussed above make a small fraction of our full sample.

The *UVJ* selection criteria also confirms that the great majority (> 98%) of our sample can be classified as active. There is also a general trend where rest-frame colours become bluer with increasing redshift implying that our high-z samples are likely comprised of less dusty systems. This could be attributed to sample bias as dusty systems would result in fainter emission-line fluxes leaving behind the less dusty and observationally bright systems (e.g., Hayashi et al. 2013). This leads to the caveat that the samples are not fully comparable across redshift as we will be missing the dustier systems. On the other hand, this could also indicate that there is a redshift evolution in the *UVJ* plane for which galaxies at high-z tend to have bluer rest-frame colours. As these galaxies evolve and their star-formation efficiency decreases and the amount of dust increases, their *UVJ* colours become redder. This is consistent with the Milky Way progenitor evolution study of Papovich et al. (2015).

4.2 Stellar Mass Functions

In this section, we present the stellar mass function (SMF) of line emitters up to $z \sim 3$ (we exclude the $z = 4.69$ [OII] emitters since we could not constrain the SMF due to the small sample size). All samples used to measure the SMF have a common $L/L_\star(z)$ cut ($0.4L_\star(z)$ and $0.85L_\star(z)$ for Hβ+[OIII] and [OII], respectively) in order to make them comparable (tracing a similar galaxy population). The observed measurements are shown in Figures 3. All the measurements have been completeness and filter profile corrected as described in §3.3. We fit the observed binned data to the Schechter function in log-form:

$$\Phi(M)\mathrm{d}M = \phi_\star \ \ln 10 \left(\frac{M}{M_\star}\right)^{1+\alpha} e^{-(M/M_\star)} \mathrm{d}\log_{10} M \qquad (3)$$

where $\phi_\star$ is the normalization, $M_\star$ is the characteristic mass, and α is the faint-end slope. The fits are plotted in Figures 3 with the fitted parameters shown in Table 2. Note that we also placed a $L/L_\star(z)$ limit as discussed at the end of §3.3 to make all our samples comparable to one another (tracing the same type of emitters).

We initially measure the faint-end slope for our deepest samples and compare them to those measured in the literature (Pérez-González et al. 2008; Marchesini et al. 2009; Muzzin et al. 2013). Based on these three studies that trace the SMF evolution up to $z \sim 5$, the faint-end slope does not evolve strongly. Therefore, to be comparable from sample to sample and also to the literature when making our comparisons, we fix $\alpha = -1.3$ and refit for $\phi_\star$ and $M_\star$ (shown in Table 2). Note that our measured α for the Hβ+[OIII] $z = 0.84$ and $z = 1.42$ SMFs and the [OII] $z = 1.47$ SMF are in agreement with the fixed α constraint as shown in Table 2.

4.2.1 Hβ+[OIII] SMFs: z = 0.84 - 3.24

We show on the left panel of Figure 3 the Hβ+[OIII] SMFs from $z = 0.84$ to 3.24 with the corresponding binned measurements and the 1σ confidence area. The tabulated measurements are shown in Table A1. We find a strong evolution in $M_\star$ where the characteristic mass increases from $z = 3.24$ to 1.42 and then varies slowly by $z = 0.84$. This is also accompanied by an evolution in $\phi_\star$ where the normalization increases from $z = 3.24$ to 1.42 and, just like $M_\star$, changes very little to $z = 0.84$. From the viewpoint of the cosmic SFR evolution, we are most likely seeing the rapid build-up of stellar mass between $z = 3.24$ and $z = 1.42$, followed by the decrease in stellar mass growth by $z = 0.84$ as star-formation activity in galaxies declines. We note that this could also be caused by the Hβ+[OIII] selection picking up different populations across cosmic time, particularly due to the change in the typical ionization parameter (see §4.4.3).

We compare our results with the *UVJ*-selected SF SMFs of Muzzin et al. (2013), *NUVrJ*-selected SF SMFs of Ilbert et al. (2013), and *Spitzer* IRAC selected SF SMFs of Pérez-González et al. (2008). Not surprisingly (due to different selection), we find that our measurements, in terms of $\phi_\star$ and $M_\star$, are in disagreement with those from the literature. The only exception is the $z = 1.45$ measurement of Pérez-González et al. (2008), which is in agreement within 1σ of our $z = 1.42$ measurement. As stated above, we fixed $\alpha = -1.3$ based on the faint-end slope measurements from the studies mentioned above. The discrepancy is most likely based on sample selection as our sample is narrow-band selected and will select different population types in comparison to attempts at mass-selected samples such as Pérez-González et al. (2008), Ilbert et al. (2013), or Muzzin et al. (2013).

We also compared our measurements to the HiZELS Hα SMFs of Sobral et al. (2014). We find that there is still discrepancies between our $\phi_\star$ and $M_\star$ and those of Sobral et al. (2014). For the overlapping $z = 0.84$, 1.42, and 2.23 samples, we find disagreements in both $\phi_\star$ and $M_\star$. This discrepancy can be attributed to population differences since the Hα samples of Sobral et al. (2014) cover the full range of star-forming galaxies (see Oteo et al. 2015). The issue could be that our Hβ+[OIII] samples (especially at higher redshifts) are missing the dustier, starburst galaxies as shown in Figure 2 where we find that the rest-frame *UVJ* colours are bluer with increasing redshift.

4.2.2 [OII] SMFs: z = 1.47 - 3.34

Figure 3 presents the [OII] SMFs from $z = 1.47$ to 3.34 with the highlighted regions showing the 1σ confidence area. The tabulated measurements are shown in Table A2. We find that there is a strong evolution in $\phi_\star$ and a constant $M_\star$ for all three redshifts sampled. The quick increase in the SMFs as shown in Figure 3 could be evidence of the build-up of stellar masses due to an increase in star-forming activity towards the peak of cosmic star-formation.

Table 2. Our fitted Schechter parameters of our stellar mass functions. Shown are the parameters when α is free and also in the case when we fix α to -1.3 in order to make our measurements comparable with the literature. Note that only the $z = 0.84$ and 1.42 Hβ+[OIII] measurements and $z = 1.47$ [OII] measurements are used for the case of α being free. This is because the sample size was large enough to probe the faint-end slope, which is then used in comparison to the literature to set a fixed α for all redshift samples. We show the Schechter parameters for where α is free only for our most populated samples. Stellar mass densities are calculated by fully integrating the stellar mass functions. Also included is the $L/L_\star(z)$ limit used to make all the samples compatible for comparison.

z	$\log_{10}\phi_\star$ (Mpc^{-3})	$\log_{10} M_\star$ ($M_\odot$)	α	$\log_{10}\phi_{\alpha=-1.3}$ (Mpc^{-3})	$\log_{10} M_{\star,\alpha=-1.3}$ ($M_\odot$)	$\log_{10}\rho_{\star,\alpha=-1.3}$ ($M_\odot$ Mpc^{-3})
Hβ+[OIII]-selected Stellar Mass Function Properties ($L/L_\star(z) > 0.4$)						
0.84	$-3.77^{+0.16}_{-0.20}$	$11.49^{+0.30}_{-0.17}$	$-1.27^{+0.06}_{-0.07}$	$-3.87^{+0.06}_{-0.11}$	$11.60^{+0.29}_{-0.13}$	$7.62^{+0.20}_{-0.08}$
1.42	$-3.88^{+0.12}_{-0.16}$	$11.53^{+0.17}_{-0.09}$	$-1.28^{+0.07}_{-0.08}$	$-3.90^{+0.05}_{-0.07}$	$11.55^{+0.12}_{-0.08}$	$7.76^{+0.07}_{-0.06}$
2.23	...	...	...	$-4.16^{+0.05}_{-0.07}$	$11.22^{+0.11}_{-0.07}$	$7.18^{+0.06}_{-0.05}$
3.24	...	...	...	$-4.16^{+0.08}_{-0.08}$	$10.96^{+0.15}_{-0.08}$	$6.90^{+0.07}_{-0.06}$
[OII]-selected Stellar Mass Function Properties ($L/L_\star(z) > 0.85$)						
1.47	$-3.88^{+0.13}_{-0.13}$	$11.59^{+0.16}_{-0.09}$	$-1.29^{+0.06}_{-0.07}$	$-3.92^{+0.05}_{-0.05}$	$11.62^{+0.10}_{-0.09}$	$7.74^{+0.06}_{-0.06}$
2.25	...	...	...	$-4.48^{+0.07}_{-0.09}$	$11.58^{+0.20}_{-0.08}$	$7.21^{+0.10}_{-0.08}$
3.34	...	...	...	$-5.18^{+0.09}_{-0.13}$	$11.58^{+0.26}_{-0.11}$	$6.51^{+0.16}_{-0.09}$

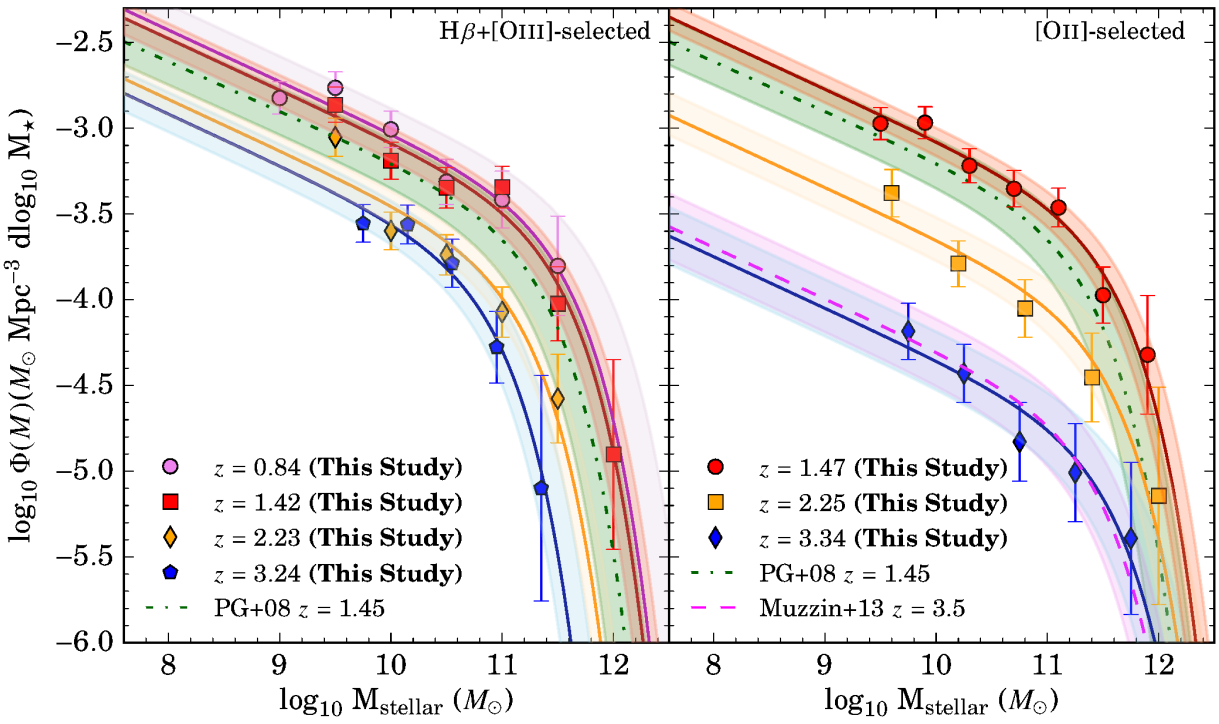
Hβ+[OIII]-selected
[OII]-selected
log10 Φ(M)(M⊙ Mpc−3 dlog10 M⋆)
log10 Mstellar (M⊙)
z = 0.84 (This Study)
z = 1.42 (This Study)
z = 2.23 (This Study)
z = 3.24 (This Study)
PG+08 z = 1.45
z = 1.47 (This Study)
z = 2.25 (This Study)
z = 3.34 (This Study)
PG+08 z = 1.45
Muzzin+13 z = 3.5

Figure 3. *Left:* Hβ+[OIII] stellar mass functions and its evolution from $z \sim 0.84$ to $z \sim 3.24$ for emission-line selected sources. We find that around the $z \sim 2-3$, there is no significant evolution until $z < 2$. *Right:* [OII] stellar mass functions between $z = 1.47$ and 3.34. For [OII], we find a strong, increasing evolution with increasing redshift in $\phi_\star$ while Hβ+[OIII] varies little. We also find that $M_\star$ is strongly decreasing with increasing redshift for Hβ+[OIII] and is relatively constant between $z \sim 1.47$ to 3.34 for [OII].

In comparison to the measurements from the literature, we find that we are in agreement with the Ultra-VISTA/COSMOS measurements of Muzzin et al. (2013) where they measure a $z = 3.5$ SMF with $\phi_\star = 10^{-5.10\pm0.11}$ Mpc^{-3} and $M_\star = 10^{11.47\pm0.07}$ $M_\odot$ in comparison to our $z = 3.34$ SMF with $\phi_\star = 10^{-5.19^{+0.09}_{-0.13}}$ Mpc^{-3} and $M_\star = 10^{11.58^{+0.26}_{-0.11}}$ $M_\odot$ (within 1σ agreement). Note that Muzzin et al. (2013) fixed $\alpha = -1.3$ (the same that we used in fitting the SMFs). We also find agreement with the *Spitzer* IRAC-selected, star-forming $z = 1.45$ SMF of Pérez-González et al. (2008) where

they find a $\phi_\star = 10^{-3.96\pm0.09}$ Mpc^{-3} and $M_\star = 10^{11.40\pm0.10}$ M$_\odot$ with $\alpha = -1.29 \pm 0.08$ (corrected from Salpeter to Chabrier IMF) in comparison to our $z = 1.47$ SMF with $\phi_\star = 10^{-3.92\pm0.05}$ Mpc^{-3} and $M_\star = 10^{11.62^{+0.10}_{-0.09}}$ M$_\odot$.

We also compare to the HiZELS Hα SMF of Sobral et al. (2014) to the overlapping $z = 1.47$ and $z = 2.25$ measurements. As in the Hβ+[OIII]-Hα comparison, we find discrepancies when comparing $\phi_\star$ and $M_\star$. This discrepancy most likely arises from the Hα sample tracing the full star-forming population, while the [OII] sample could include potential LINERs (low [OIII]/Hβ ratios equates to lower [OII] luminosities) and bright emitters as potential AGNs. Despite this contamination, [OII] has been shown to be a reliable star-forming indicator[4](e.g., Hayashi et al. 2015) and to test whether LINERs and AGNs may be contributing to this discrepancy will require spectroscopic follow-up.

4.3 Evolution of Stellar Mass Densities

We infer the stellar mass densities (SMDs) by integrating the stellar mass functions for the full mass range:

$$\rho_\star = \int_0^\infty M\Phi(M)\mathrm{d}M = \phi_\star M_\star \Gamma(2+\alpha) \quad (4)$$

where $\rho_\star$ is the stellar mass density, $\phi_\star$ is the normalization, $M_\star$ is the characteristic stellar mass, and α is the faint-end slope. We report the SMDs in Table 2 for all of our samples.

Our measurements are shown in Figure 4 for both Hβ+[OIII] and [OII] up to $z \sim 3.3$. We find that for $z \sim 3.3$ to $z \sim 1.5$, both samples of line emitters shown an increase in stellar mass build-up. This is consistent with the view that galaxies were producing stars at an increasing rate up to $z \sim 2$. In the case of [OII], our assessment of the SMD ends here as we have no $z < 1.5$ [OII] measurements.

We also find that our Hβ+[OIII] and [OII] measurements at $z \sim 1.5$ and ~ 2.2, respectively, are in good agreement. For the $z \sim 3.3$ measurements, we find a discrepancy between the Hβ+[OIII] and [OII] measurements where the separation is ~ 0.4 dex. This discrepancy could be attributed to a sample bias due to the different $L_\star(z)$ cuts that were applied ($0.4L_\star(z)$ and $0.85L_\star(z)$ for Hβ+[OIII] and [OII], respectively) or even number statistics (since the [OII] $z = 3.34$ is the smallest sample being comprised of only 35 emitters, while the Hβ+[OIII] sample contains 179 emitters).

Figure 4 also presents a comparison to the full population (star-forming + quiescent) literature compilation of Madau & Dickinson (2014). We also highlight the IRAC-selected full sample of Pérez-González et al. (2008), and the COSMOS/UltraVISTA K_s-band measurements of Ilbert et al. (2013) and Muzzin et al. (2013). We note that these samples have measurements for the star-forming population, although these mass-selected samples are divided by using a colour-colour selection(s) (e.g., UVJ) to separate the quiescent and star-forming populations. We instead use the full population literature measurements as a way to qualitatively gauge the evolution of the star-forming fraction of galaxies.

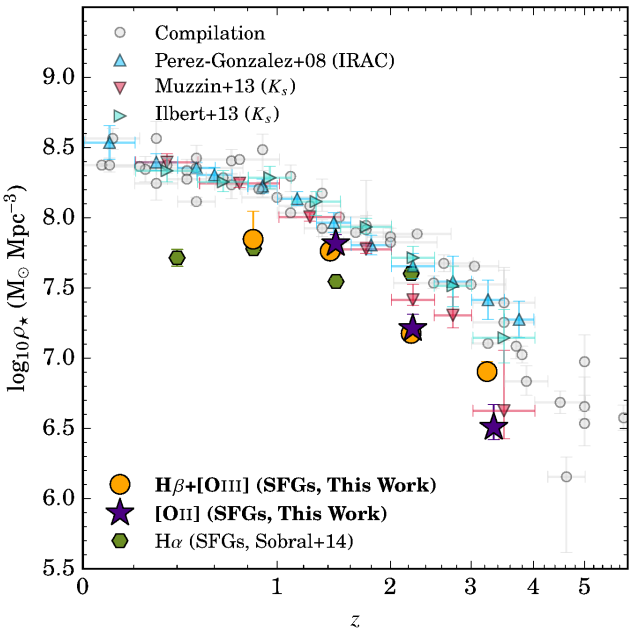

Figure 4. The cosmic stellar mass density evolution of our Hβ+[OIII] and [OII] sample. Overlaid are the full population (star-forming + quiescent) measurements from the Madau & Dickinson (2014) compilation. We also highlight the Pérez-González et al. (2008), Ilbert et al. (2013), and Muzzin et al. (2013) SMD measurements. We find that our measurements match the general picture of a fast stellar mass build-up from $z \sim 3.3$ to $z \sim 1$. By $z \sim 1$, we find that our measurements diverge from the full population literature measurements, implying that star-formation activity in emission-line selected galaxies is decreasing resulting in a slower stellar mass assembly growth and a population transition from star-forming/active to quiescent/passive systems.

Also shown on Figure 4 are the SMD measurements of the HiZELS Hα sample from Sobral et al. (2014). We find that our measurements are consistent with the literature in the sense that all our measurements are implying a stellar mass build-up all the way to $z = 0.84$. In comparison to the SMD compilation of Madau & Dickinson (2014) and the measurements of Pérez-González et al. (2008), Ilbert et al. (2013), and Muzzin et al. (2013), we find that our Hβ+[OIII] and [OII] SMDs are all below the literature, which is expected as these are for a subset ("active" galaxies) of the total population of galaxies. From $z \sim 3$ to ~ 1.5, this gap diminishes implying that the star-formation fraction increases up to $z \sim 1.5$ where it then decreases until $z \sim 0.8$ as the gap increases. In comparison to the HiZELS Hα measurements of Sobral et al. (2014), we find that we are in agreement for the $z \sim 0.84$ Hβ+[OIII] sample. At all other redshifts, we are not in agreement, but this is due to sample biases where at $z = 1.47$ our Hβ+[OIII] and [OII] samples probe ~ 0.30 and ~ 0.17 dex deeper in line luminosity, respectively, than the Hα measurements. For the $z = 2.23$ measurements, our

[4] This is still a matter of debate as the [OII] line is also metallicity dependent (e.g., Kewley et al. 2004). A recent study by Darvish et al. (2015b) used a sample of 58 spectroscopically-confirmed $z \sim 0.53$ star-forming galaxies and found that the dust- and metallicity-corrected SFR([OII]) was consistent up to ~ 0.02 dex with SFR(Hβ). Future spectroscopic measurements of $z > 1$ are needed to reliably ascertain the nature of [OII] as a star-formation indicator.

Hβ+[OIII] and [OII] measurements are at the same line luminosity depth as the Hα measurements of Sobral et al. (2014). The inconsistency could then be attributed to the evolution of the emission lines itself.

We note that this evolution (especially at higher redshifts) could be a byproduct of the change in the physical conditions that produce these lines. Therefore, it is important to keep in mind when interpreting the results shown in Figure 4 that other variables (e.g., electron densities, ionization parameter, gas abundances, metal absorption, etc.) can affect and/or drive the evolution (e.g., Nakajima & Ouchi 2014; Hayashi et al. 2015). With this in mind, it becomes apparent that we must study the physical conditions of the ISM for which these lines originate from. We do this in the following sections by investigating the EW_{rest} evolution for each emission line, as well as the observational proxy of the ionization parameter ([OIII]/[OII]) and its evolution over cosmic time.

Parameters of the Power-Law $EW_{rest} \propto M^{\beta}$				
z	Emitter	β	$\log_{10}$ Norm.	$\log_{10}$ Norm. (β fixed)
0.84	Hβ+[OIII]	-0.33 ± 0.02	4.72 ± 0.14	4.89 ± 0.01
1.42	Hβ+[OIII]	-0.33 ± 0.03	5.33 ± 0.32	5.53 ± 0.02
2.23	Hβ+[OIII]	-0.38 ± 0.06	6.20 ± 0.61	5.87 ± 0.04
3.24	Hβ+[OIII]	-0.43 ± 0.04	6.66 ± 0.38	5.78 ± 0.03
1.47	[OII]	-0.23 ± 0.01	3.79 ± 0.12	3.84 ± 0.01
2.25	[OII]	-0.48 ± 0.04	6.90 ± 0.44	6.63 ± 0.03
3.34	[OII]	-0.41 ± 0.04	6.58 ± 0.45	6.97 ± 0.04
4.69	[OII]	-0.49 ± 0.04	6.97 ± 0.44	6.57 ± 0.03

Table 3. Shown are the fitted parameters of the power-law that relates EW_{rest} to $M_{stellar}$. We run two different fits: one for which both parameters are free and the other where $\beta = -0.35$ and -0.45 for Hβ+[OIII] and [OII], respectively. This is to ensure compatibility between samples and mitigation of the bias from selection effects when looking at the evolution of the normalization. The only exception is the $z = 1.47$ [OII], which is fitted for a constant $\beta = -0.23$ as this better fits the data.

4.4 Equivalent Widths of Hβ+[OIII] and [OII] Emitters

4.4.1 Equivalent Width – $M_{stellar}$ Relation

Fumagalli et al. (2012) and Sobral et al. (2014) have both shown a power-law relationship between the median EW_{rest}(Hα) and $M_{stellar}$, as well as an increasing evolution in the normalization. This signifies that for every mass bin, the median EW_{rest} for Hα increases with redshift. We extend this analysis for our Hβ+[OIII] and [OII] sample and measure the EW_{rest}-$M_{stellar}$ relationship up to $z \sim 5$.

The EW_{rest} are calculated using Equation 1. Note that no dust correction has been applied to the line and continuum fluxes as we assume that $E(B-V)_{nebular} \sim E(B-V)_{stellar}$. The credibility of assuming that the reddening of the nebular is equivalent to that of the stellar continuum is still in debate. Calzetti et al. (2000) finds $E(B-V)_{nebular} = 2.27E(B-V)_{stellar}$ for which other studies have reached the same conclusion (e.g., Förster Schreiber et al. 2009; Wild et al. 2011; Wuyts et al. 2011; Hemmati et al. 2015). Kashino et al. (2013) measured $E(B-V)_{nebular} = 1.20E(B-V)_{stellar}$ using a sample of 271 sBzK-selected, spectroscopically confirmed Hα sources as part of the FMOS-COSMOS survey. Using 3D-*HST* grism spectroscopic measurements of 79 $z \sim 1$ *Herschel*-selected main sequence star-forming galaxies, Puglisi et al. (2016) measured $E(B-V)_{nebular} = 1.07E(B-V)_{stellar}$. Recently, Shivaei et al. (2015) used a sample of 262 spectroscopically confirmed $z \sim 2$ star-forming galaxies from the MOSDEF survey and concluded that, on average, $E(B-V)_{nebular} = E(B-V)_{stellar}$, although they find it to dependent on SFR. Reddy et al. (2015) came to a similar conclusion that $E(B-V)_{nebular} - E(B-V)_{stellar} = -0.049 + 0.079/\xi$, where $\xi = 1./(\log_{10}[\mathrm{sSFR(SED)/yr^{-1}}] + 10)$. Due to the conflicting measurements in the literature, we find that a change in our initial assumption would result in our EW_{rest} measurements systematically changing by a factor of $-0.4k(\lambda)[E(B-V)_{nebular} - E(B-V)_{stellar}]$ dex, where $k(\lambda)$ is the dust attenuation curve.

Figure 5 shows the full sample with the binned measurements. Because of the significant scatter, each of the binned data points represent the median EW_{rest} and the 1σ errors are measured via bootstrapping to incorporate the errors due to scattering. Based on the actual data points and the binned data, we can see a linear trend such that the EW_{rest} is increasing with decreasing stellar mass. This is also seen in the Hα studies of Fumagalli et al. (2012) and Sobral et al. (2014). We also highlight in Figure 5 the EW_{rest} cut which was used in the initial selection of narrow-band colour excess (Sobral et al. 2013a). For the Hβ+[OIII] $z > 1$ and [OII] $z > 2$ samples, this selection does not have an effect on the medians calculated since their EW_{rest} are much higher than the EW_{rest} selection limit. Although, the line flux-limit is more important for our high-z samples as the effect would be the lack of fainter emission-line sources which consequentially leads to sources with lower EW_{rest}. For our Hβ+[OIII] $z = 0.84$ and [OII] $z = 1.47$ samples, the EW_{rest} limit affects the median EW_{rest} measured beyond a set mass range. We then only show median EW_{rest} measurements below 10^{10} $M_{\odot}$ for Hβ+[OIII] and 10^{11} $M_{\odot}$ for [OII].

As in Fumagalli et al. (2012) and Sobral et al. (2013a), we find that the median EW_{rest}-$M_{stellar}$ relationship is best fitted with a power-law of the form $EW_{rest} \propto M^{\beta}$, where M is the stellar mass and β is the power-law slope. Table 3 shows the fitted parameters for each sample. We notice that for all Hβ+[OIII] samples, $\beta \sim -0.35$ which is somewhat higher than the $\beta = -0.25 \pm 0.01$ measured by Sobral et al. (2014) for their Hα samples. This is also consistent with the 3D-*HST* $1.1 < z < 1.5$ $\beta = -0.38$ of Fumagalli et al. (2012). The normalization is found to increase with increasing redshift and flatten out by $z = 3.24$. For the [OII] samples, we find that the $z = 1.47$ is consistent with $\beta = -0.23 \pm 0.01$ while the $z > 1.5$ samples have $\beta \sim -0.45$. This is consistent with the $z = 0.53$ spectroscopic [OII] measurement of Darvish et al. (2015b) where they find $\beta = -0.47 \pm 0.06$. We find the normalization increases up to $z = 3.34$ then seems to drop by $z = 4.69$.

We note that this evolution is affected by systematic effects arising from selection biases. Since our sample is both EW_{rest}-limited and luminosity-limited, we then miss lower-mass sources ($M < 10^{8.5}$ $M_{\odot}$) due to the luminosity-limit, and higher-mass sources ($M > 10^{10}$ $M_{\odot}$; for $z = 0.84$ Hβ+[OIII]) due to the EW_{rest} cut at a fixed SFR. To test how the selection effects can affect our results, we use our most populated and deep samples (Hβ+[OIII] $z = 0.84$ and [OII] $z = 1.47$)

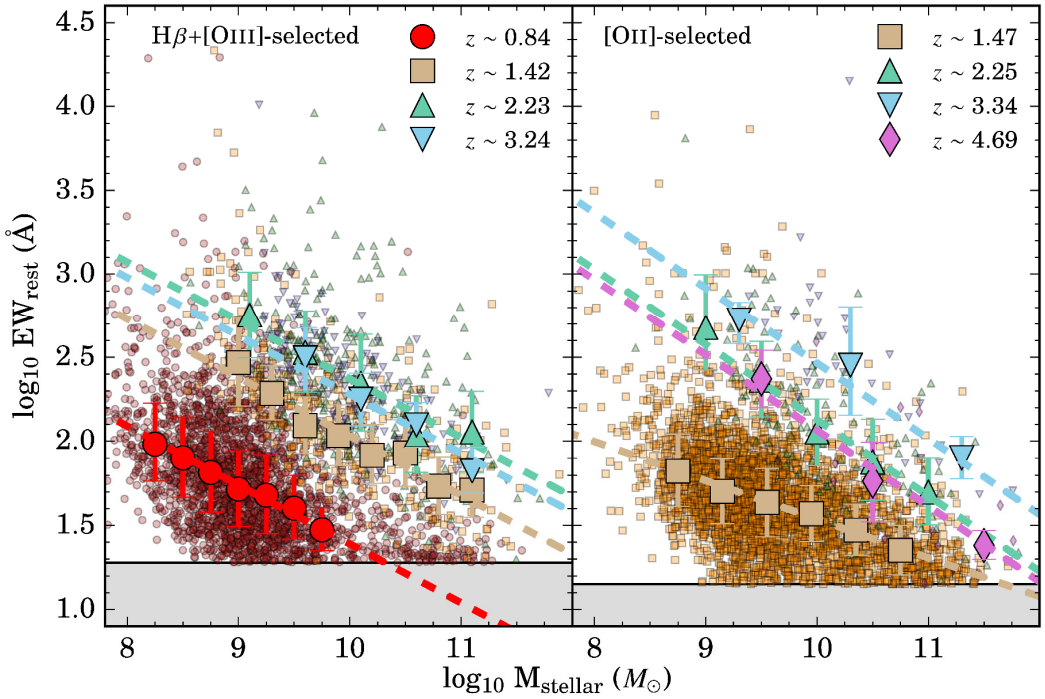

Figure 5. Shown is a scatter plot of the EW_{rest} versus $M_{stellar}$ for all our samples. We also include, as larger symbols, the median EW_{rest} for given stellar mass bins. Highlighted in *grey* is the EW_{rest} limit, which results in an incompleteness in our sample for the high-mass sources. This effect is only seen in the Hβ+[OIII] $z = 0.84$ sample and to some extent in the [OII] $z = 1.47$ sample. For the other high-z samples, the EW_{rest} limit does not cause any incompleteness in the high-mass end as we do not probe high enough masses (low EW_{rest}) for which it must be considered.

and apply luminosity limits between $10^{40.4}$ to $10^{41.7}$ erg s^{-1} in increments of 0.1 dex and fit the same power-law to the sample. We then look at the variations in β and the normalization as a function of the luminosity limit. We find that as the luminosity limit increases, β becomes steeper while the normalization increases. This is expected since the two are not independent from each other. As the luminosity limit increases, then more sources with low-mass will be removed such that the median EW_{rest} increases more towards lower masses, resulting in β becoming steeper and the normalization increasing.

Because of this degeneracy, we then repeat the same methodology with β fixed to -0.35 and -0.45 for all Hβ+[OIII] and [OII] samples, respectively, (except for the [OII] $z = 1.47$ where $\beta = -0.23$) and fit for the normalization as a function of the luminosity limit. We find that the normalization does not change more than < 0.1 dex for Hβ+[OIII] and < 0.01 dex for [OII].

The fit is shown in Table 3 and Figure 5. We find that the normalization evolution is in fact real and implies that with increasing redshift, the median EW_{rest} for a given stellar mass increases up to $z = 2.23$ for Hβ+[OIII] and for our [OII] sample up to $z = 3.34$.

4.4.2 Evolution of Equivalent Widths with Redshift

Based on the normalization seen in the EW_{rest}-$M_{stellar}$ relationship, we study the evolution of the normalization and compare with measurements from the literature. Figure 6 shows the evolution of the median EW_{rest} for our Hβ+[OIII] and [OII] measurements. For each measurement, we make a correction for the skewness of the mass distribution per each measurement. Since we select a specific mass range between $10^{9.5} < \log_{10} M < 10^{10.0}$ M$_\odot$[5], we ideally would want the median stellar mass of each of our measurements to be equal to $10^{9.75}$ M$_\odot$. This is not always the case such that the stellar mass distribution is skewed from a normal distribution. Because of the dependency between EW_{rest} and $M_{stellar}$, not correcting for the skewness in the distribution would result in systematic increases/decreases in the measured median EW_{rest} (corresponding to the mean stellar mass measured). To correct for this, we measure the mean mass for each sample and compute the inferred EW_{rest} from the corresponding fit. We then compute based on the fit what the median EW_{rest} should be at the center of the mass bin ($10^{9.75}$ M$_\odot$) and then subtract both measurements to get a correction factor. The result is that the median EW_{rest} increases/decreases (~ 0.1 dex) based on whether the mean mass was above/below $10^{9.75}$ M$_\odot$.

Included in Figure 6 are the Hβ+[OIII] measurements from the literature (Labbé et al. 2013; Schenker et al. 2013;

[5] We select this mass range to be consistent with the $z > 5$ studies (e.g, Labbé et al. 2013; Smit et al. 2014; Rasappu et al. 2015; Smit et al. 2015) and also because it corresponds to the peaks in our stellar mass distributions as shown in Figure 1.

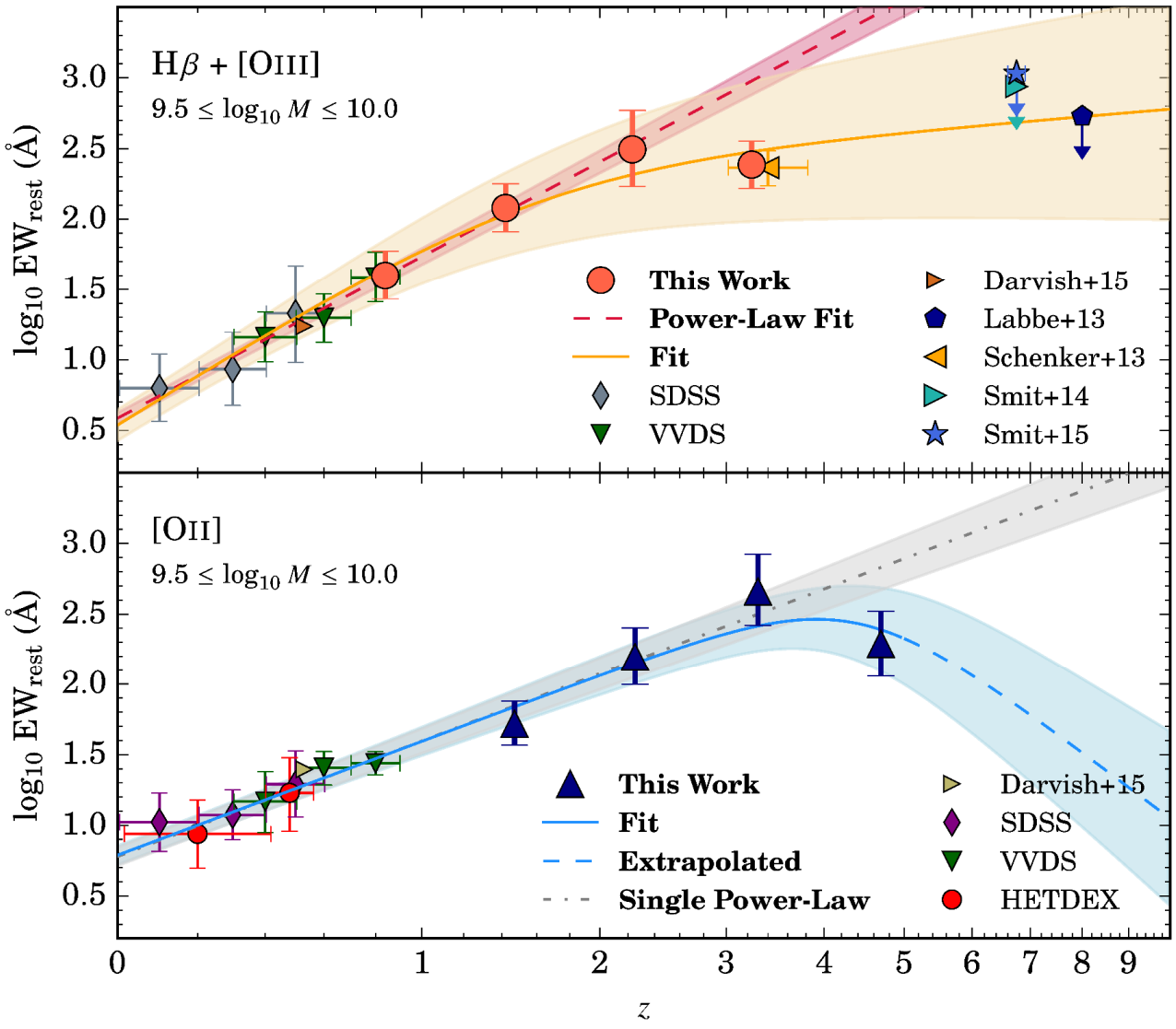

Figure 6. Presented is the EW_{rest} evolution for sources that have $9.5 < \log 10 M_{stellar} < 10$ $M_{\odot}$. We also include measurements from the literature to constrain the low-z end and to compare to our extrapolated fits in the high-z regime. We fit single power-law and mixed power-law functions (combination of two power-laws) to our measurements and those from the literature. Included for each fit is the shaded 1σ region. We find that the EW_{rest} evolution for Hβ+[OIII] flattens out to $z > 5$ and the [OII] drops in this regime. In terms of the ionization state of the gas, we find that the EW_{rest} evolution of both emission-lines hints to a harder ionizing source, although other factors such as metallicities and abundances can affect the evolution as well.

Smit et al. 2014, 2015). To ensure a constrained $EW_{rest}(z = 0)$, we compute the median EW_{rest} from the SDSS-III/BOSS-DR12 spectroscopic sample Thomas et al. (2013) by selecting only emission-lines with $EW_{rest} > 3$ Å to ensure that the measured EW_{rest} is not dominated by uncertainties in the stellar continuum subtraction (Fumagalli et al. 2012) and all galaxies that were classified as star-forming based on the BPT diagram. The VVDS catalog of Lamareille et al. (2009) was also included where only galaxies identified as star-forming were selected. We also include the [OIII] $z \sim 0.53$ EW_{rest} measurements from the Keck DEIMOS spectroscopic sample of Darvish et al. (2015b).

For the [OII] sample, we also compute the median EW_{rest} from the HETDEX survey (Adams et al. 2011; Bridge et al. 2015) and remove any sources with X-ray detection found by Bridge et al. (2015) to eliminate AGN contamination. We also include the [OII] $z \sim 0.53$ EW_{rest} measurements from Darvish et al. (2015b). Figure 7 shows the Hα EW_{rest} evolution found in the literature (Erb et al. 2006; Fumagalli et al. 2012; Sobral et al. 2014; Rasappu et al. 2015; Faisst et al. 2016) in comparison to the EW_{rest} evolu-

Power-Law Fit Parameters					
Sample	Model	$EW_{rest}(z=0)$ (Å)	γ	ϵ	c
Hβ+[OIII]	Single	3.85 ± 0.34	3.81 ± 0.14	...	...
Hβ+[OIII]	Mixed	3.53 ± 0.90	4.53 ± 0.63	3.93 ± 0.47	2.57 ± 0.46
[OII]	Single	6.00 ± 0.90	2.72 ± 0.19	...	...
[OII]	Mixed	6.14 ± 0.95	2.68 ± 0.25	8.09 ± 1.38	5.35 ± 0.54
Hα	Single	21.14 ± 2.54	1.82 ± 0.20	...	...

Table 4. Measurements of the Power-Law Parameters. Two different models were used to fit the data. Those listed as "single" refer to a single power-law of the form $(1+z)^{\gamma}$ and those listed as "mixed" refer to the model as defined in Equation 5.

tion of the Hβ+[OIII] and [OII] samples. We selected a mass range of $10^{9.5} < M < 10^{10.0}$ $M_{\odot}$ for all determinations of the EW_{rest} evolution. Changing the mass range used in Figures 6 and 7 only changes the normalization because of the power law relationship shown in Figure 5. Furthermore, all errors presented in Figure 6 and 7 for our sample and the SDSS, VVDS, and HETDEX determined measurements are based on a bootstrapping assessment to calculate the 95% confidence intervals.

To ensure that all the literature data is consistent and comparable with our data set, we correct the literature measurements to match our IMF (convert from the literature-assumed IMF to Chabrier (2003) IMF) and also cover the same mass range ($10^{9.5} < M < 10^{10.0}$ $M_{\odot}$). We also make another correction for the $z > 5$ Hβ+[OIII] literature data points (Labbé et al. 2013; Smit et al. 2014, 2015) as described in Appendix D to take into account the contribution of Hβ in the total EW_{rest} measured in these studies.

We fit the evolution of the EW_{rest} (z) to a mix of power-laws of the form:

$$EW_{rest}(z) = EW_{rest}(z=0)\frac{(1+z)^{\gamma}}{1+[(1+z)/c]^{\epsilon}} \quad (5)$$

where γ and ϵ are the power-law slopes. This functional form is similar to that used by Madau & Dickinson (2014) to model the cosmic SFRD evolution. For the Hβ+[OIII] sample, we only use our measurements, our SDSS and VVDS determinations, and the upper limits set by Labbé et al. (2013) and Smit et al. (2014, 2015) to constrain the fit. For the [OII] sample we use our measurements, the SDSS and VVDS determinations, and the HETDEX measurements. The fitted parameters are shown in Table 4 for our sample of Hβ+[OIII] and [OII] emitters, as well as the HiZELS Hα sample from Sobral et al. (2014), which was further constrained by the SDSS and VVDS data. We also overlay the fits and their 1σ error range on Figure 6. Note that we also fit a simple power-law of the form $(1+z)^{\gamma}$. This functional form has been shown to work for the Hα EW_{rest} evolution (e.g., Fumagalli et al. 2012; Sobral et al. 2014; Rasappu et al. 2015; Marmol-Queralto et al. 2015).

As shown in Figure 6, a single power-law would match our Hβ+[OIII] measurements and others drawn from the literature up to $z \sim 2$. For $z > 2$, a single power-law model would pass above the upper limits set by Smit et al. (2014, 2015) and Labbé et al. (2013) hinting that the slope becomes shallower and deviates from a simple power-law form. Also, our $z = 3.24$ and the $z \sim 3.5$ measurement of Schenker et al. (2013) both provide evidence that the evolution becomes shallower. The change in the slope of the EW_{rest} evolution has also been recently detected by Marmol-Queralto et al. (2015) where they use grism spectroscopy of the Hα line from the 3D-*HST* survey and samples of spectroscopically confirmed and photometric-redshift selected galaxies from CANDELS within the redshift interval $1 < z < 5$. Faisst et al. (2016) also reports a change in the power-law slope with increasing redshift up to $z \sim 6$ where the power-law deviates from $(1+z)^{1.8}$ to $(1+z)^{1.3}$. We use the mixed power-law model shown in Equation 5 to incorporate the deviation from a single power-law and fit to our measurements, the SDSS determinations, the $z \sim 3.5$ measurements of Schenker et al. (2013), and the upper limits set by Labbé et al. (2013) and Smit et al. (2014, 2015). We find that the model defined in Equation 5 better fits the observed measurements.

The lower panel of Figure 6 shows the [OII] EW_{rest} evolution up to $z \sim 5$, along with measurements from HETDEX, VVDS, SDSS, and Darvish et al. (2015b). Our measurements are the first that cover the $z \sim 1.5$ to 5 range allowing us to compare to the $z < 1$ regime. We initially fit to a single power-law and find that the [OII] evolution increases up to $z \sim 3$. There is some evidence in our measurements for a drop from $z \sim 3$ to ~ 5, but more measurements have to be made in the $z > 3$ regime in order to confirm the decreasing evolution. To incorporate this drop seen between our $z = 3.34$ and $z = 4.69$ measurements, we fit using the model described in Equation 5.

Our Hβ+[OIII] and [OII] fits using the mixed power-law model described in Equation 5 are shown in Figure 6 with the measured parameters described in Table 4. We find an increasing evolution in the EW_{rest}(Hβ+[OIII]) and EW_{rest}([OII]) up to $z \sim 2-3$. The Hβ+[OIII] evolution trend becomes shallower from $z \sim 2$ to higher z. This is constrained by our $z \sim 2.23$ and ~ 3.34 measurements, the $z \sim 3.5$ measurement of Schenker et al. (2013), and the recent measurements of Labbé et al. (2013) and Smit et al. (2014, 2015). The literature measurements can be interpreted as upper limits since they require a significant excess in the *Spitzer* IRAC bands to be detected. But this assumes that the UV is bright enough that the highest EW sources are detected. Based on this interpretation, we can constrain the high-z end using our $z > 2$ measurements with the condition that the fit cannot exceed the upper limits.

Beyond $z > 3$, we find some evidence that the EW_{rest}([OII]) is decreasing to higher z. Currently, there are no other measurements in the literature that cover this redshift regime. Our EW_{rest}([OII]) measurements are the first presented in the literature at these redshifts for which we can assess the cosmic evolution of the [OII] equivalent width. Future studies from the next-generation of telescopes and space observatories will better constrain the EW_{rest}([OII]) evolution. Based on our results, we can conclude that there is some evidence of a decrease in the EW_{rest}([OII]) for $z > 3$. It may not be surprising then that high-z UV studies (e.g., Smit et al. (2014, 2015)) do not find strong evidence for [OII] but do find [OIII] since, based on our measurements and the mixed power-law fits, the [OII] EW_{rest} is significantly lower than [OIII]. This could be due to a combination of changes in the oxygen abundances and ionization state of the gas.

We also show in Figure 7 the comparison of the EW_{rest}(Hα) evolution, measured from the HiZELS Hα sample of Sobral et al. (2014), with our EW_{rest}(Hβ+[OIII]) and EW_{rest}([OII]) measured evolution. We find that based on the

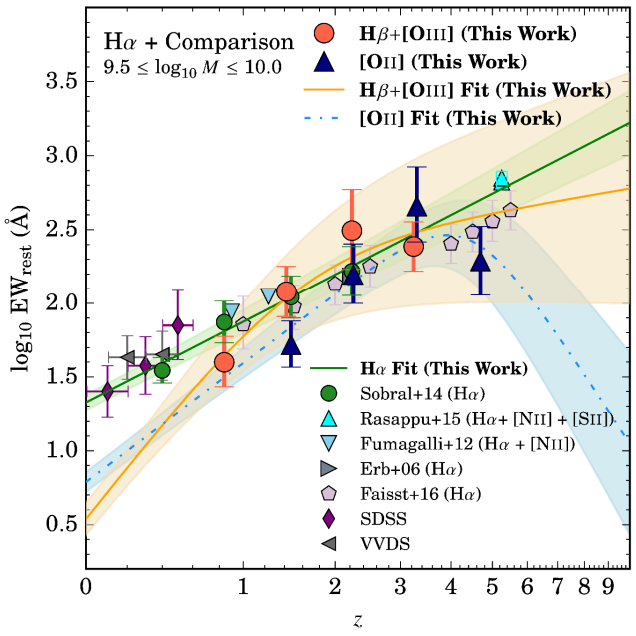

Figure 7. The EW_{rest} evolution of major rest-frame optical emission lines within $9.5 < \log_{10} M_{stellar} < 10$ $M_\odot$. We include our empirical fits of the Hβ+[OIII] and [OII] EW_{rest} evolution in order to study how the EW_{rest} evolves per nebular emission-line. We find that the Hβ+[OIII] EW_{rest} drops faster from high-z to low-z than the other emission-lines. This is followed by [OII] and then by Hα such that the Hβ+[OIII] EW_{rest} at $z = 0$ is weaker compared to [OII], which is also weaker than Hα. The drops are in order of higher to lower ionization potentials such that in the low-z Universe, higher ionization potential lines have lower EW_{rest} relative to low ionization potential lines. We also find that the Hβ+[OIII] EW_{rest} is much higher than [OII] for $z > 5$, implying a Universe with extreme ionizing sources that easily can produce the [OIII] line.

fits, EW_{rest}(Hβ+[OIII]) drops from high to low-z the fastest, followed by [OII] and then by Hα. In terms of the required ionization potentials to form these lines, it is then not surprising that the EW_{rest}(Hβ+[OIII]) drops the fastest since it requires a harder ionizing source (photons with $\approx$ 35.12 eV) to cause a strong [OIII] line. This is then followed by [OII] ($\approx$ 13.62 eV) and Hα ($\approx$ 13.60 eV) in decreasing order of required ionization potentials. From a broader point-of-view, the EW_{rest} decline in order of ionization potentials matches the current view of cosmic star-formation activity which has been in decline for the $\sim$ 11 Gyr. A decrease in star formation rates results in the decrease of bright, massive stars that can create UV photons to form the emission lines we observe. Although other factors, such as metallicities, densities, electron temperatures, and abundances can also play a crucial role in the decrease of the EW_{rest}.

4.4.3 Evolution of the Ionization State

We have shown in Figures 6 and 7 the evolution in the three major nebular emission-lines associated with star-formation to high-z. Based on this evolution, we investigate how the [OIII]/[OII] ratio changes with redshift. The [OIII]/[OII] line ratio is an important observational proxy of the ionization state of the gas since the [OIII] line has a higher ionization potential compared to the [OII] line and has been used in many studies in the literature (e.g., Nakajima et al. 2013; Nakajima & Ouchi 2014; Hayashi et al. 2015). We note that the [OIII]/[OII] line ratio is also dependent on stellar mass and metallicity (e.g., Kobulnicky & Kewley 2004; Liu et al. 2008; Hayashi et al. 2015; Kewley et al. 2015). To properly understand the dependency of [OIII]/[OII] with the ionization parameter, stellar mass, gas-phase abundances and metallicities requires spectroscopic follow-up. In this section, we present our analysis of the [OIII]/[OII] evolution in terms of the evolution in the ionization parameter but caution the reader that other factors affect this evolution as well.

If we assume that our Hβ+[OIII] samples are primarily [OIII] emitters (see discussion in §3.4), then we can take our observed Hβ+[OIII] and [OII] EW_{rest} and measure the ratio to determine [OIII]/[OII]. We take the ratios of the equivalent widths rather than the ratios of the emission lines as the dependency on dust correction is eliminated with the assumption that $E(B-V)_{nebular} \sim E(B-V)_{stellar}$ (see discussion in §4.4.1 on how this assumption affects the results). An issue that arises is that the continuum flux at rest-frame 3727Å and 5007Å may not be equivalent/similar. To test how this can affect our measurements of [OIII]/[OII], we compare the EW_{rest}([OIII])/EW_{rest}([OII]) and the $F_{[OIII]}/F_{[OII]}$ line ratios from the SDSS-III/BOSS-DR12 (Thomas et al. 2013) and VVDS (Lamareille et al. 2009) catalogs. This comparison is shown in Appendix E. We find that using the EW_{rest} to measure [OIII]/[OII] is consistent, on average, with using the line fluxes with a negligible systematic offset arising from the differing continuum fluxes (-0.06 and -0.04 dex for SDSS and VVDS, respectively; see Figure E1).

Figure 8 shows the [OIII]/[OII] evolution with our observational measurements at $z = 1.47$ and 2.25 along with measurements we computed from SDSS-III/BOSS-DR12 (Thomas et al. 2013) and VVDS (Lamareille et al. 2009; Le Fèvre et al. 2013). We also include the $z \sim 2.3$ measurement of MOSDEF (Sanders et al. 2016)[6], the $z \sim 1.5$ measurement of Hayashi et al. (2015), and the $z \sim 1.7$ measurement of Rigby et al. (2011). We exclude our $z = 3.34$ measurement due to the [OII] sample size (13 sources) being ~ 5 times smaller in comparison to the Hβ+[OIII] sample size (62 sources) which would make the two samples incomparable. Overall, our measurements combined with those from the literature show that the [OIII]/[OII] ratio is increasing up to $z \sim 3$ such that at higher redshifts the ionizing source was much harder. When we compare our measurements with those within the same redshift range, we find that we are within 1σ agreement. We note that the literature measurements are for the mass range $9.5 < \log_{10} M < 10.0$ $M_\odot$.

We fit the evolution of the [OIII]/[OII] ratio to a power-law of the form:

$$[\mathrm{OIII}]/[\mathrm{OII}] = [\mathrm{OIII}]/[\mathrm{OII}](z = 0)(1+z)^{\eta} \quad (6)$$

[6] The Sanders et al. (2016) measurement was recomputed to only cover the $9.5 < \log_{10} M < 10.0$ $M_\odot$ since [OIII]/[OII] is also a function of stellar mass (e.g., Hayashi et al. 2015). We recompute their [OIII]/[OII] measurement and calculate the errors via bootstrapping. The measurement cited in Sanders et al. (2016) is $\log_{10}$ [OIII]/[OII] $= 0.10^{+0.37}_{-0.11}$.

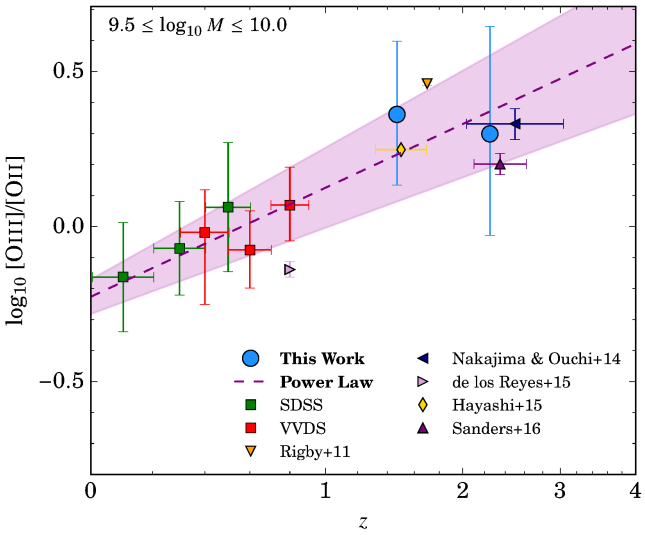

Figure 8. Shown is the [OIII]/[OII] evolution. Included are measurements from SSDS and VVDS, as well as other spectroscopic measurements from the literature. We find that the [OIII]/[OII] increases with redshift suggesting a harder ionizing source at higher redshifts. Although, we note that evolution in the metallicity and abundances can also influence the [OIII]/[OII] evolution. In terms of the ionizing source, the [OIII]/[OII] evolution shown here explains why recent studies have detected emission lines that require high ionization potentials at $z > 6$ (e.g., Vanzella et al. 2010; Sobral et al. 2015a; Stark et al. 2015a,b).

where we find [OIII]/[OII]($z = 0$) = 0.59 ± 0.07 (normalization) and $\eta = 1.17 \pm 0.24$ (power-law slope). We only use the SDSS, VVDS, and our measurements to fit for the power-law. The fit along with the 1σ region is shown in Figure 8 and matches well with the observed data points not used in the fitting process. Based on our power-law model, the [OIII]/[OII] ratio is predicted to continue to increase with redshift. This matches with the fits shown on Figure 6 where we find that the evolution of EW_{rest}(Hβ+[OIII]) becomes shallower and the EW_{rest}([OII]) drops significantly. The situation could be that the hardness of the ionizing source increases when going back in cosmic time such that the production of an [OII] emission-line is suppressed as electrons in doubly-ionized oxygen are unable to transition to lower energy levels when bombarded by highly energetic photons and free electrons. We note that this can also be the byproduct of changing metallicities and abundances. The physical source of this is still in debate, but lower amounts of metal coolants and dust, higher star formation activity and efficiency, and even changes in the initial mass function can influence the hardness of the ionizing source.

Our results for the [OIII]/[OII] evolution and its extrapolation to $z > 3$ can also explain why recent spectroscopic observations are able to find emission-lines from high ionization potential transitions (e.g., CIII], CIV, NIV, HeII). Stark et al. (2014) spectroscopically observed 17 $z \sim 2$ gravitationally-lensed galaxies to find strong NIV], OIII], CIV, SiIII], and CIII] emission-lines requiring photons with energies > 47 eV, much higher than the local Universe. Their argument is using such emission-lines that require high ionization energies could be used in conjunction with Lyα to study reionization. This led to the spectroscopic detection of NIV ($z = 5.56$; Vanzella et al. 2010), CIII] ($z \sim 6-7$; Stark et al. 2015a), and CIV ($z = 7.045$; Stark et al. 2015b) emitters, such that the ionizing source is much harder with increasing redshift. An even more extreme case is the recent discovery of HeII in the COSMOS Redshift 7 (CR7) source (Sobral et al. 2015b). To produce this emission line requires ionizing photons with energy ~ 54 eV and has been attributed to the presence of PopIII stars or direct collapse black holes (e.g., Pallottini et al. 2015; Dijkstra et al. 2016; Visbal et al. 2016). The following studies comprise a handful of sources but match our extrapolation of the [OIII]/[OII] evolution to show that the ionization potential increases with redshift. Future studies using the next-generation space-based observatories (e.g., *JWST*) could spectroscopically observe the traditional optical emission-lines for $z > 5$ (falls in observer-frame infrared) and assess the ionization state of the gas with better accuracy. For now, we present our extrapolated $z > 3$ results as a prediction that can be tested by future high-z studies.

5 CONCLUSIONS

We have presented the evolution of the stellar mass functions and densities up to $z \sim 3$, the evolution of the rest-frame equivalent widths up to $z \sim 5$, and the evolution of the ionization parameter as described by the [OIII]/[OII] ratio up to $z \sim 3$. The main results of this study are the following:

(i) In conjunction with the widely used *UVJ* colour-colour classification scheme, we find that $\sim 98\%$ of all Hβ+[OIII] and [OII] emitters are classified as "active" (star-forming or AGN) galaxies.

(ii) The stellar mass functions of Hβ+[OIII] emitters show a strong, increasing evolution in $M_\star$ from $10^{10.96^{+0.15}_{-0.08}}$ $M_\odot$ to $10^{11.60^{+0.29}_{-0.13}}$ $M_\odot$ and a weak, decreasing evolution in $\phi_\star$ from $10^{-3.87^{+0.06}_{-0.11}}$ Mpc^{-3} to $10^{-4.16\pm0.08}$ Mpc^{-3} with increasing redshift. The opposite trends are seen for the stellar mass functions of [OII] emitters from $z = 1.47$ to $z = 3.34$ where an unchanging $M_\star \sim 10^{11.60}$ $M_\odot$ is seen for all redshifts sampled and a strong, increasing evolution in $\phi_\star$ from $10^{-5.18^{+0.09}_{-0.13}}$ Mpc^{-3} to $10^{-3.92\pm0.05}$ Mpc^{-3} with decreasing redshift.

(iii) The similarity between the $z = 0.84$ and 1.42 Hβ+[OIII] SMFs and the rise in the SMFs between $z = 3.24$ to $z = 1.42$ is probable evidence for the rapid stellar mass build-up followed by its decay due to the decrease of star-formation activity in the Universe. The stellar mass functions of the [OII] emitters all shows rapid build-up of stellar masses from $z = 3.34$ to $z = 1.47$ for [OII]-selected galaxies.

(iv) Stellar mass densities of our Hβ+[OIII] and [OII] emitters, in conjunction with the HiZELS Hα SMDs of Sobral et al. (2014), show how the evolution in the SMDs traces that of the full sample (passive + active) as found in the literature. By $z = 0.84$, we find that the SMDs deviate from the full population implying the transition of active galaxies into passive galaxies. This ties into the picture of decreasing star-formation activity in the Universe.

(v) The relationship between EW_{rest} and stellar mass for Hβ+[OIII] and [OII] emitters up to $z \sim 3$ and ~ 5, respec-

tively, is studied for the first time where we find a power-law relationship between the two physical properties as seen in Hα studies (e.g., Fumagalli et al. 2012; Sobral et al. 2014). We find that all our Hβ+[OIII] samples are best represented by $EW_{rest} \propto M^{-0.35}$ and the [OII] samples as $\propto M^{-0.45}$. The $z = 1.47$ [OII] sample has a shallower trend best fit as $\propto M^{-0.23}$.

(vi) We find that the Hβ+[OIII] EW_{rest} increases from $z = 0$ to $z \sim 2$ by a factor of ~ 100. From $z \sim 2$ to ~ 8, we find evidence for a shallower trend by using the *Spitzer* IRAC measurements of Labbé et al. (2013) and Smit et al. (2014, 2015) as upper limits and also the deviation from the $z = 0 - 2$ power-law seen by our $z = 3.24$ EW_{rest} and the $z \sim 3.5$ Keck/MOSFIRE EW_{rest} measurement of Schenker et al. (2013).

(vii) We present the first measurement of the [OII] EW_{rest} out to $z \sim 5$. We find that the [OII] EW_{rest} increases by a factor of ~ 60, followed by a decrease in EW_{rest} to higher redshift. This could be one reason why no high-z measurements of [OII] exists in the $z > 5$ regime from UV studies that are finding ubiquitous high Hβ+[OIII] EW sources.

(viii) We study the evolution of the ionization state of the gas using the [OIII]/[OII] line ratio. The line ratio increases beyond $z \sim 3$ such that the higher the redshift, the harder the ionizing source. This could explain the lack of [OII] detections at high-z. The harder ionizing source (e.g., high energy photons coming from massive stars) could suppress the [OII] line while producing a stronger [OIII] line as the doubly-ionized oxygen atoms are bombarded with highly energetic photons and free electrons such that they can not make the transition to produce an [OII] line. The harder ionizing source can also explain the recent detections of emission lines with high ionization potentials at $z \sim 5$ to ~ 7 (e.g., CIII], CIV, HeII, NIV). The physical reason for a harder ionizing source is still in debate and can be explained as changes in the amount of metal coolants, dust, star-formation activity and efficiency, and possibly even a varying initial mass function.

Our results present a clearer picture of the EW_{rest} of the Hβ+[OIII] and [OII] lines, as well as an understanding of how the strengths of these lines and its dependency on the changes in the ionization state of the gas can explain the recent developments in detecting Hβ+[OIII] at $z \sim 6 - 8$ and other emission lines that arise from transitions involving high ionization potentials. The results highlighted in this paper prepare for the next-generation of ground-based telescopes (e.g., Thirty Meter Telescope) and state-of-the-art space-based observatories (e.g., *JWST*, *EUCLID*, *WFIRST*) by presenting an outline of the evolution of the EW_{rest} and the [OIII]/[OII] line ratio and predictions for the high-z Universe that can better our understanding of the physical conditions for which forms the observed EW_{rest} and [OIII]/[OII] line ratios.

ACKNOWLEDGMENTS

We thank Philip Best, Rychard Bouwens, Naveen Reddy, Irene Shivaei, and Anahita Alavi for their insightful discussions and comments. The catalogs used in this analysis are publicly available from Sobral et al. (2013a).

DS acknowledges financial support from the Netherlands Organisation for Scientific research (NWO) through a Veni fellowship, from FCT through a FCT Investigator Starting Grant and Start-up Grant (IF/01154/2012/CP0189/CT0010) and from FCT grant PEst-OE/FIS/UI2751/2014. IRS acknowledges support from ST7C (ST/L00075X/1), the ERC Advanced Grant DUSTYGAL (321334) and a Royal Society/Wolfson Merit award. BD acknowledges financial support from NASA through the Astrophysics Data Analysis Program (ADAP), grant number NNX12AE20G. JPS gratefully acknowledges support from a Hintze Research Fellowship.

REFERENCES

Adams J. J., et al., 2011, ApJS, 192, 5
Arnouts S., et al., 2007, A&A, 476, 137
Baldry I. K., Balogh M. L., Bower R. G., Glazebrook K., Nichol R. C., Bamford S. P., Budavari T., 2006, MNRAS, 373, 469
Bauer A. E., et al., 2013, MNRAS, 434, 209
Behroozi P. S., Wechsler R. H., Conroy C., 2013, ApJ, 770, 57
Best P., et al., 2013, Astrophysics and Space Science Proceedings, 37, 235
Bielby R., et al., 2012, A&A, 545, A23
Bolzonella M., et al., 2010, A&A, 524, A76
Bongiorno A., et al., 2010, A&A, 510, A56
Bouwens R. J., et al., 2012a, ApJ, 752, L5
Bouwens R. J., et al., 2012b, ApJ, 754, 83
Bouwens R. J., et al., 2015, ApJ, 803, 34
Bradshaw E. J., et al., 2013, MNRAS, 433, 194
Brammer G. B., et al., 2011, ApJ, 739, 24
Bridge J. S., et al., 2015, ApJ, 799, 205
Bruzual G., Charlot S., 2003, MNRAS, 344, 1000
Bundy K., et al., 2006, ApJ, 651, 120
Calzetti D., Armus L., Bohlin R. C., Kinney A. L., Koornneef J., Storchi-Bergmann T., 2000, ApJ, 533, 682
Capak P., et al., 2007, ApJS, 172, 99
Caputi K. I., Cirasuolo M., Dunlop J. S., McLure R. J., Farrah D., Almaini O., 2011, MNRAS, 413, 162
Chabrier G., 2003, PASP, 115, 763
Charlot S., Fall S. M., 2000, ApJ, 539, 718
Cirasuolo M., et al., 2007, MNRAS, 380, 585
Coil A. L., et al., 2011, ApJ, 741, 8
Conroy C., Wechsler R. H., 2009, ApJ, 696, 620
Cucciati O., et al., 2012, A&A, 539, A31
Daddi E., Cimatti A., Renzini A., Fontana A., Mignoli M., Pozzetti L., Tozzi P., Zamorani G., 2004, ApJ, 617, 746
Damen M., Labbé I., Franx M., van Dokkum P. G., Taylor E. N., Gawiser E. J., 2009, ApJ, 690, 937
Darvish B., Mobasher B., Sobral D., Scoville N., Aragon-Calvo M., 2015a, ApJ, 805, 121
Darvish B., Mobasher B., Sobral D., Hemmati S., Nayyeri H., Shivaei I., 2015b, ApJ, 814, 84
Davé R., Oppenheimer B. D., Finlator K., 2011, MNRAS, 415, 11
Davé R., Finlator K., Oppenheimer B. D., 2012, MNRAS, 421, 98
Davidzon I., et al., 2015, preprint, (arXiv:1511.01145)
Dijkstra M., Gronke M., Sobral D., 2016, preprint, (arXiv:1602.07695)
Drory N., Alvarez M., 2008, ApJ, 680, 41
Erb D. K., Steidel C. C., Shapley A. E., Pettini M., Reddy N. A., Adelberger K. L., 2006, ApJ, 647, 128

Faisst A. L., et al., 2016, preprint, (arXiv:1601.07173)
Förster Schreiber N. M., et al., 2009, ApJ, 706, 1364
Fumagalli M., et al., 2012, ApJ, 757, L22
Furlong M., et al., 2015, MNRAS, 450, 4486
Gallazzi A., Brinchmann J., Charlot S., White S. D. M., 2008, MNRAS, 383, 1439
Garilli B., et al., 2014, A&A, 562, A23
Geach J. E., Smail I., Best P. N., Kurk J., Casali M., Ivison R. J., Coppin K., 2008, MNRAS, 388, 1473
Giodini S., et al., 2012, A&A, 538, A104
González V., Labbé I., Bouwens R. J., Illingworth G., Franx M., Kriek M., Brammer G. B., 2010, ApJ, 713, 115
González V., Labbé I., Bouwens R. J., Illingworth G., Franx M., Kriek M., 2011, ApJ, 735, L34
González V., Bouwens R., Illingworth G., Labbé I., Oesch P., Franx M., Magee D., 2014, ApJ, 781, 34
Grazian A., et al., 2015, A&A, 575, A96
Gruppioni C., et al., 2013, MNRAS, 432, 23
Hayashi M., Sobral D., Best P. N., Smail I., Kodama T., 2013, MNRAS, 430, 1042
Hayashi M., et al., 2015, PASJ, 67, 80
Hemmati S., Mobasher B., Darvish B., Nayyeri H., Sobral D., Miller S., 2015, ApJ, 814, 46
Henriques B. M. B., White S. D. M., Thomas P. A., Angulo R., Guo Q., Lemson G., Springel V., Overzier R., 2015, MNRAS, 451, 2663
Ilbert O., et al., 2009, ApJ, 690, 1236
Ilbert O., et al., 2010, ApJ, 709, 644
Ilbert O., et al., 2013, A&A, 556, A55
Kajisawa M., et al., 2009, ApJ, 702, 1393
Karim A., et al., 2011, ApJ, 730, 61
Kashino D., et al., 2013, ApJ, 777, L8
Kewley L. J., Geller M. J., Jansen R. A., 2004, AJ, 127, 2002
Kewley L. J., Zahid H. J., Geller M. J., Dopita M. A., Hwang H. S., Fabricant D., 2015, ApJ, 812, L20
Khostovan A. A., Sobral D., Mobasher B., Best P. N., Smail I., Stott J. P., Hemmati S., Nayyeri H., 2015, MNRAS, 452, 3948
Kobulnicky H. A., Kewley L. J., 2004, ApJ, 617, 240
Labbé I., et al., 2013, ApJ, 777, L19
Lamareille F., et al., 2009, A&A, 495, 53
Lawrence A., et al., 2007, MNRAS, 379, 1599
Le Fèvre O., et al., 2013, A&A, 559, A14
Lee K.-S., et al., 2012, ApJ, 752, 66
Li C., White S. D. M., 2009, MNRAS, 398, 2177
Lilly S. J., et al., 2007, ApJS, 172, 70
Liu X., Shapley A. E., Coil A. L., Brinchmann J., Ma C.-P., 2008, ApJ, 678, 758
Madau P., Dickinson M., 2014, ARA&A, 52, 415
Marchesini D., van Dokkum P. G., Förster Schreiber N. M., Franx M., Labbé I., Wuyts S., 2009, ApJ, 701, 1765
Marmol-Queralto E., McLure R. J., Cullen F., Dunlop J. S., Fontana A., McLeod D. J., 2015, preprint, (arXiv:1511.01911)
McLure R. J., et al., 2013, MNRAS, 428, 1088
Mobasher B., et al., 2015, ApJ, 808, 101
Mortlock A., et al., 2015, MNRAS, 447, 2
Moustakas J., et al., 2013, ApJ, 767, 50
Muzzin A., et al., 2013, ApJ, 777, 18
Nakajima K., Ouchi M., 2014, MNRAS, 442, 900
Nakajima K., Ouchi M., Shimasaku K., Hashimoto T., Ono Y., Lee J. C., 2013, ApJ, 769, 3
Nayyeri H., et al., 2014, ApJ, 794, 68
Newman S. F., et al., 2014, ApJ, 781, 21
Noeske K. G., et al., 2007, ApJ, 660, L47
Oke J. B., Gunn J. E., 1983, ApJ, 266, 713
Oteo I., Sobral D., Ivison R. J., Smail I., Best P. N., Cepa J., Pérez-García A. M., 2015, MNRAS, 452, 2018
Pallottini A., et al., 2015, MNRAS, 453, 2465
Papovich C., et al., 2015, ApJ, 803, 26
Peng Y.-j., et al., 2010, ApJ, 721, 193
Pérez-González P. G., et al., 2008, ApJ, 675, 234
Pozzetti L., et al., 2010, A&A, 523, A13
Puglisi A., et al., 2016, A&A, 586, A83
Rasappu N., Smit R., Labbe I., Bouwens R., Stark D., Ellis R., Oesch P., 2015, preprint, (arXiv:1509.02167)
Reddy N. A., Pettini M., Steidel C. C., Shapley A. E., Erb D. K., Law D. R., 2012, ApJ, 754, 25
Reddy N. A., et al., 2015, ApJ, 806, 259
Rigby J. R., Wuyts E., Gladders M. D., Sharon K., Becker G. D., 2011, ApJ, 732, 59
Rodriguez-Gomez V., et al., 2015, preprint, (arXiv:1511.08804)
Sanders R. L., et al., 2016, ApJ, 816, 23
Schaerer D., de Barros S., 2009, A&A, 502, 423
Schaerer D., de Barros S., 2010, A&A, 515, A73
Schenker M. A., Ellis R. S., Konidaris N. P., Stark D. P., 2013, ApJ, 777, 67
Scoville N., et al., 2007, ApJS, 172, 1
Shim H., Chary R.-R., Dickinson M., Lin L., Spinrad H., Stern D., Yan C.-H., 2011, ApJ, 738, 69
Shirazi M., Brinchmann J., Rahmati A., 2014, ApJ, 787, 120
Shivaei I., Reddy N. A., Steidel C. C., Shapley A. E., 2015, ApJ, 804, 149
Smit R., et al., 2014, ApJ, 784, 58
Smit R., et al., 2015, ApJ, 801, 122
Sobral D., et al., 2009, MNRAS, 398, 75
Sobral D., Best P. N., Smail I., Geach J. E., Cirasuolo M., Garn T., Dalton G. B., 2011, MNRAS, 411, 675
Sobral D., Best P. N., Matsuda Y., Smail I., Geach J. E., Cirasuolo M., 2012, MNRAS, 420, 1926
Sobral D., Smail I., Best P. N., Geach J. E., Matsuda Y., Stott J. P., Cirasuolo M., Kurk J., 2013a, MNRAS, 428, 1128
Sobral D., et al., 2013b, ApJ, 779, 139
Sobral D., Best P. N., Smail I., Mobasher B., Stott J., Nisbet D., 2014, MNRAS, 437, 3516
Sobral D., et al., 2015a, MNRAS, 451, 2303
Sobral D., Matthee J., Darvish B., Schaerer D., Mobasher B., Röttgering H. J. A., Santos S., Hemmati S., 2015b, ApJ, 808, 139
Sobral D., Stroe A., Koyama Y., Darvish B., Calhau J. a., Afonso A., Kodama T., Nakata F., 2016, MNRAS,
Somerville R. S., Davé R., 2015, ARA&A, 53, 51
Stark D. P., Ellis R. S., Bunker A., Bundy K., Targett T., Benson A., Lacy M., 2009, ApJ, 697, 1493
Stark D. P., Schenker M. A., Ellis R., Robertson B., McLure R., Dunlop J., 2013, ApJ, 763, 129
Stark D. P., et al., 2014, MNRAS, 445, 3200
Stark D. P., et al., 2015a, MNRAS, 450, 1846
Stark D. P., et al., 2015b, MNRAS, 454, 1393
Steidel C. C., et al., 2014, ApJ, 795, 165
Stott J. P., et al., 2013, MNRAS, 436, 1130
Stott J. P., et al., 2014, MNRAS, 443, 2695
Stott J. P., et al., 2016, MNRAS, 457, 1888
Stroe A., Sobral D., 2015, MNRAS, 453, 242
Swinbank A. M., Smail I., Sobral D., Theuns T., Best P. N., Geach J. E., 2012, ApJ, 760, 130
Thomas D., et al., 2013, MNRAS, 431, 1383
Tomczak A. R., et al., 2014, ApJ, 783, 85
Vanzella E., et al., 2010, A&A, 513, A20
Visbal E., Haiman Z., Bryan G. L., 2016, preprint, (arXiv:1602.04843)
Vulcani B., et al., 2015, preprint, (arXiv:1509.00486)
Wild V., Charlot S., Brinchmann J., Heckman T., Vince O., Pacifici C., Chevallard J., 2011, MNRAS, 417, 1760
Williams R. J., Quadri R. F., Franx M., van Dokkum P., Labbé I., 2009, ApJ, 691, 1879
Wuyts S., et al., 2011, ApJ, 738, 106

Yabe K., Ohta K., Iwata I., Sawicki M., Tamura N., Akiyama M., Aoki K., 2009, ApJ, 693, 507
da Cunha E., Charlot S., Elbaz D., 2008, MNRAS, 388, 1595
de Barros S., Schaerer D., Stark D. P., 2014, A&A, 563, A81
van Dokkum P. G., et al., 2010, ApJ, 709, 1018

APPENDIX A: STELLAR MASS FUNCTIONS

Table A1. Hβ+[OIII]-selected stellar mass function. Shown are the stellar mass bins ($\log_{10} M$), the number of sources per bin (#), the observed ($\Phi_{\rm obs}$) and final ($\Phi_{\rm final}$) stellar mass distribution per stellar mass bin, and the comoving volume per bin. $\Phi_{\rm final}$ includes the completeness, EW, and filter profile corrections.

$\log_{10} M$ ($M_\odot$)	#	$\Phi_{\rm obs}$ (Mpc^{-3} d$\log_{10}$M)	$\Phi_{\rm final}$ (Mpc^{-3} d$\log_{10}$M)	Volume (10^5 Mpc^3)
z = 0.84				
9.00±0.25	185	−2.95	−2.82 ± 0.09	3.33
9.50±0.25	185	−2.95	−2.76 ± 0.09	3.33
10.00±0.25	64	−3.42	−3.01 ± 0.10	3.33
10.50±0.25	23	−3.86	−3.31 ± 0.13	3.33
11.00±0.25	11	−4.18	−3.42 ± 0.17	3.33
11.50±0.25	3	−4.74	−3.80 ± 0.29	3.33
z = 1.42				
9.50±0.25	111	−3.03	−2.86 ± 0.10	2.37
10.00±0.25	80	−3.40	−3.19 ± 0.11	4.06
10.50±0.25	54	−3.57	−3.35 ± 0.12	4.06
11.00±0.25	44	−3.66	−3.34 ± 0.12	4.06
11.50±0.25	8	−4.40	−4.02 ± 0.22	4.06
12.00±0.25	1	−5.31	−4.90 ± 0.55	4.06
z = 2.23				
9.50±0.25	74	−3.26	−3.05 ± 0.11	2.72
10.00±0.25	77	−3.83	−3.60 ± 0.11	10.45
10.50±0.25	53	−4.00	−3.74 ± 0.12	10.68
11.00±0.25	22	−4.39	−4.07 ± 0.15	10.68
11.50±0.25	5	−5.03	−4.58 ± 0.26	10.68
z = 3.24				
9.75±0.20	50	−3.88	−3.56 ± 0.11	9.38
10.15±0.20	49	−3.93	−3.56 ± 0.11	10.47
10.55±0.20	19	−4.34	−3.79 ± 0.14	10.47
10.95±0.20	6	−4.84	−4.28 ± 0.21	10.47
11.35±0.20	1	−5.62	−5.10 ± 0.66	10.47

APPENDIX B: STELLAR MASS COMPARISONS

The COSMOS and UDS fields both have a wealth of multi-wavelength data, which is useful when measuring the physical properties (e.g., stellar masses) of galaxies via SED fitting. Stellar masses for COSMOS includes the *i*-band selected measurements of Ilbert et al. (2010) using *Le Phare* and the UltraVISTA/COSMOS K_s-band selected measurements of Muzzin et al. (2013) using *FAST*. Our Hβ+[OIII]- and [OII]-selected samples are from both fields but we measure the stellar masses using MAGPHYS. This is to ensure that stellar masses are measured using the same SED fitting code in both fields. Not normalizing the stellar mass determinations to the same code can introduce systematic effects arising from model dependencies.

We compare our stellar mass measurements in Figure B1 to those of Ilbert et al. (2010) (*top panel*) and Muzzin et al. (2013) (*bottom panel*). Both studies used a Chabrier IMF but different SED fitting codes and sets of filters, which is the most probable reason for the scatter. To eliminate the scatter arising from redshift differences, we only show comparison measurements for which the difference between the redshift measurement in our catalogs (measured using EaZY, see Khostovan et al. 2015) and the comparison measurements is < 0.1. Overall, we find that our measurements are consistent with the literature.

Table A2. [OII]-selected stellar mass function. Same as in A1.

$\log_{10} M$ ($M_\odot$)	#	Φ_{obs} (Mpc^{-3} d$\log_{10}$ M)	Φ_{final} (Mpc^{-3} d$\log_{10}$ M)	Volume (10^5 Mpc^3)
z = 1.47				
9.50±0.20	202	−3.14	−2.97 ± 0.09	6.97
9.90±0.20	188	−3.17	−2.97 ± 0.09	6.97
10.30±0.20	94	−3.47	−3.22 ± 0.10	6.97
10.70±0.20	64	−3.64	−3.35 ± 0.11	6.97
11.10±0.20	42	−3.82	−3.46 ± 0.11	6.97
11.50±0.20	11	−4.40	−3.97 ± 0.16	6.97
11.90±0.20	2	−5.14	−4.32 ± 0.35	6.97
z = 2.25				
9.60±0.30	47	−3.48	−3.38 ± 0.14	2.36
10.20±0.30	43	−3.94	−3.79 ± 0.13	6.29
10.80±0.30	22	−4.23	−4.05 ± 0.17	6.29
11.40±0.30	7	−4.73	−4.45 ± 0.26	6.29
12.00±0.30	1	−5.58	−5.14 ± 0.63	6.29
z = 3.34				
9.75±0.25	13	−4.44	−4.18 ± 0.16	7.13
10.25±0.25	10	−4.73	−4.43 ± 0.17	10.84
10.75±0.25	5	−5.14	−4.83 ± 0.23	13.81
11.25±0.25	3	−5.36	−5.01 ± 0.29	13.81
11.75±0.25	1	−5.84	−5.39 ± 0.44	13.81

APPENDIX C: EQUIVALENT WIDTH COMPLETENESS

We incorporate a second completeness correction which deals with the EW_{rest} cut causing a loss in high-mass sources (e.g., §3.1 in Sobral et al. 2014; Figure 5). For our $z > 1$ Hβ+[OIII] and [OII], this incompleteness is not an issue since it will only affect our measurements at very high masses ($> 10^{12}$ $M_\odot$, except for [OII] $z = 1.47$ where the incompleteness arises by $> 10^{11.25}$ $M_\odot$). Our $z \sim 0.84$ Hβ+[OIII] sample is affected for masses $> 10^{10}$ $M_\odot$. The $z \sim 1.47$ [OII] sample is relatively complete up to masses for which we probe.

We correct for this incompleteness using a similar approach from Sobral et al. (2014). Since our $z > 1$ Hβ+[OIII] are complete for the full range of stellar masses (Figure 1), we use these samples as proxies in measuring the incompleteness. We start by binning up the full sample in stellar mass bins which corresponds to a median EW_{rest}. We then decrease the corresponding EW_{rest} to match the $z \sim 0.84$ median EW_{rest} stellar mass bins, which results in a number of high-mass sources removed from the full sample because of the $z = 0.84$ Hβ+[OIII] EW_{rest} cut. The correction factor is then calculated as the number of sources that are recovered relative to the total number of sources in each bin. We run these correction determinations based off the $z \sim 1.47$, 2.23, and 3.24 samples and find that for all redshifts probed in the Hβ+[OIII] sample, the EW_{rest} cut completeness correction does not evolve. To apply the completeness corrections, we extrapolate for the mass range of the $z \sim 0.84$ sample and apply the corrections accordingly. These corrections are mass dependent and range from ∼ 50% to 200% increase in $\Phi(M)$ between 10^{10} $M_\odot$ to 200% and $10^{11.5}$ $M_\odot$, respectively.

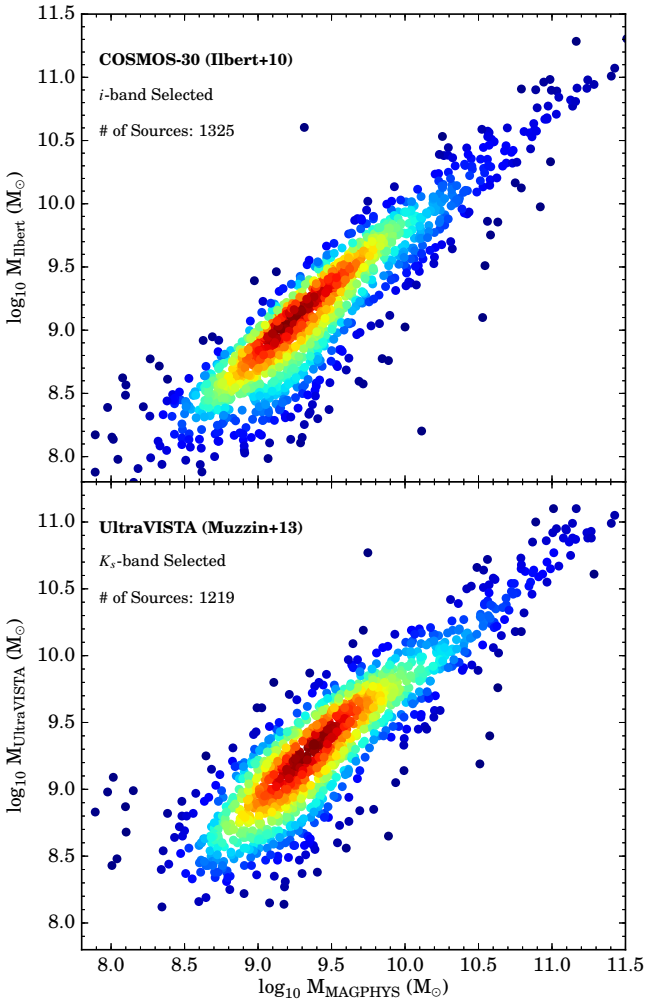

Figure B1. Present is the comparison between the stellar masses measured by Ilbert et al. (2010) (*top panel*) and Muzzin et al. (2013) (*bottom panel*) versus the stellar masses we measure using MAGPHYS. We find that, overall, our measurements are consistent with those from the comparison samples. The scatter in the measurements is most probably arising from the different sets of assumptions (e.g., SF history, metallicity range, dust prescription). We eliminate the scatter arising from differing redshifts by only comparing sources that have a $\Delta z < 0.1$, where Δz represents the difference between the photometric redshift measured by Khostovan et al. (2015) and the comparison studies.

APPENDIX D: CORRECTING $Z > 5$ Hβ+[OIII] EQUIVALENT WIDTHS

To ensure that the $z > 5$ Hβ+[OIII] literature data points (Labbé et al. 2013; Smit et al. 2014, 2015) are comparable to our measurements, we must take into account the Hβ contribution in the total EW_{rest} measured. These samples used nebular excess in the *Spitzer* IRAC bands to probe the combined Hβ4861, [OIII]4959, and [OIII]5007 lines. Our sample on the other hand consists of either Hβ, [OIII]4959, or

[OIII]5007 because the narrow-band filter is narrow enough to separate the lines, but the broad-band and photometric redshift selections used can not. As inferred in Khostovan et al. (2015), the sample is primarily [OIII]5007 for the brightest sources, but towards fainter line fluxes we start picking up more Hβ emitters. Sobral et al. (2015a) observed $z = 1.42$ Hβ+[OIII] emitters in the ~ 10 deg^2 CF-HiZELS survey and had spectroscopic measurements to differentiate between Hβ and [OIII] to find that the sample consisted of primarily [OIII]5007 emitters. To compensate for this, we reduce the EW$_{\rm rest}$ measured by Labbé et al. (2013), Smit et al. (2014), and Smit et al. (2015) by 20% based on the [OIII]/Hβ ratios from the $z \sim 2.3$ studies of the MOSDEF survey (e.g., Sanders et al. 2016).

APPENDIX E: RATIOS OF EW$_{\rm rest}$ = FLUXES?

The [OIII]/[OII] line ratio is typically measured by taking the ratio of the dust-corrected [OIII] and [OII] fluxes. In §4.4.3, we use the ratio of the EW$_{\rm rest}$ instead of the line fluxes to determine [OIII]/[OII], as this eliminates the dependency of dust corrections under the assumption that $E(B-V)_{\rm nebular} \sim E(B-V)_{\rm stellar}$ (e.g., Reddy et al. 2015; Shivaei et al. 2015). An issue that arises with this approach is that the EW$_{\rm rest}$ is a ratio between the line and continuum flux, where the continuum flux at 3727Å may not be equivalent/similar to the continuum flux at 5007Å. Therefore, we must assess how well does the EW$_{\rm rest}$([OIII])/EW$_{\rm rest}$([OII]) correlate with $F_{\rm [OIII]}/F_{\rm [OII]}$, where the only factor that can cause any systematic deviation is the difference between the continuum fluxes.

To assess this issue, we use the SDSS DR12 (Thomas et al. 2013) and VVDS (Lamareille et al. 2009) catalogs. Both are spectroscopic surveys and contain the EW$_{\rm rest}$ and line fluxes for both [OIII] and [OII], allowing us to directly measure the correlation between EW$_{\rm rest}$([OIII])/EW$_{\rm rest}$([OII]) and $F_{\rm [OIII]}/F_{\rm [OII]}$. For both catalogs, we select only sources that are confirmed to be star-forming and within the stellar mass range of $9.5 < \log_{10} M < 10.0$ M$_\odot$.

Figure E1 shows the correlation between EW$_{\rm rest}$([OIII])/EW$_{\rm rest}$([OII]) and $F_{\rm [OIII]}/F_{\rm [OII]}$. We measure the correlation in log-scale as:

$$\log_{10}\frac{\rm EW_{rest}([OIII])}{\rm EW_{rest}([OII])} = \log_{10}\frac{F_{\rm [OIII]}}{F_{\rm [OII]}} + \log_{10}\frac{f_{C,\rm [OII]}}{f_{C,\rm [OIII]}} \quad \text{(E1)}$$

where f_C is the continuum flux at the wavelength of the emission line. Therefore, a linear correlation in log-space would have the intercept equivalent to the ratio of the continuum fluxes, which would represent the systematic offset introduced by using the EW$_{\rm rest}$ ratios to measure [OIII]/[OII]. Furthermore, because we assume $E(B-V)_{\rm nebular} \sim E(B-V)_{\rm stellar}$ the dust corrections would still cancel out. Changes in this assumption would introduce a systematic factor due to dust correction and not continuum flux differences of $0.4(k_{\rm [OII]} - k_{\rm [OIII]})(E(B-V)_{\rm nebular} - E(B-V)_{\rm stellar})$ dex.

We find that for the SDSS and VVDS samples, the slope of the correlation is close to unity such that EW$_{\rm rest}$([OIII])/EW$_{\rm rest}$([OII]) $\sim F_{\rm [OIII]}/F_{\rm [OII]}$. The r-value (correlation coefficient) is ~ 0.9 for both samples which implies that the two different ratios are strongly correlated. More importantly, we find that the intercepts measured are -0.06 and -0.04 dex for SDSS and VVDS, respectively. This suggests that the systematic offset introduced by the ratio of the continuum fluxes is negligible in the determination of [OIII]/[OII] via the ratio of the EW$_{\rm rest}$.

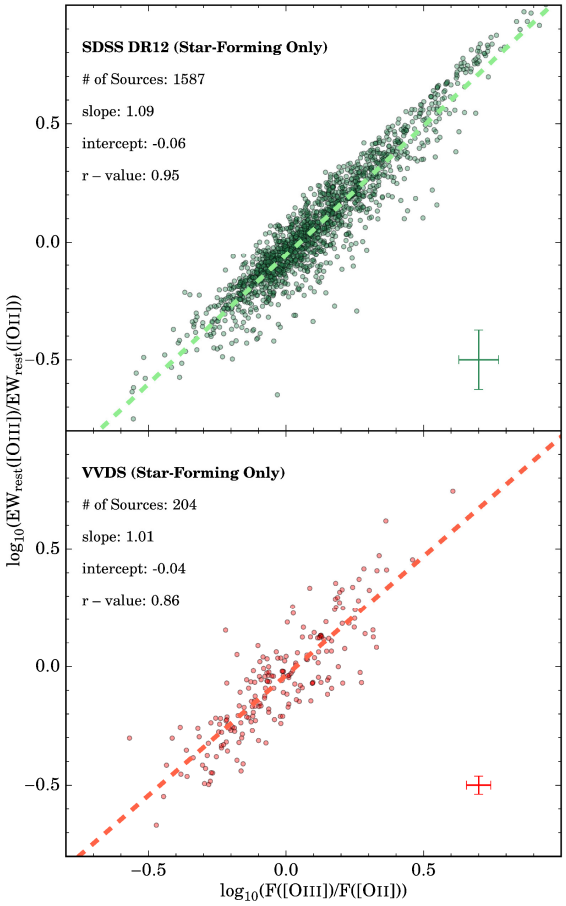

Figure E1. The comparison between the [OIII]/[OII] determined by the ratio of the EW$_{\rm rest}$ and the line fluxes in log-space. The intercept represents the ratio of the continuum fluxes. We find that the intercepts are ~ 0 and the slopes of the correlation are near unity, such that the ratio of the EW$_{\rm rest}$ directly traces the [OIII]/[OII] line ratio with negligible systematic offsets introduced by differing continuum fluxes.

This paper has been typeset from a TEX/LATEX file prepared by the author.